SAND REPORT
SAND2002-8592
Unlimited Release
Printed December 2002

Small-Scale Multiaxial Deformation Experiments on Solder for High-Fidelity Model Development

Wei-Yang Lu, T. Jesse Lim, Brad L. Boyce, J. Mark Grazier, and H. Eliot Fang

Prepared by
Sandia National Laboratories
Albuquerque, New Mexico 87185 and Livermore, California 94550

Sandia is a multiprogram laboratory operated by Sandia Corporation,
a Lockheed Martin Company, for the United States Department of Energy's
National Nuclear Security Administration under Contract DE-AC04-94-AL85000.

Issued by Sandia National Laboratories, operated for the United States Department of Energy by Sandia Corporation.

Available to DOE and DOE contractors from
U.S. Department of Energy
Office of Scientific and Technical Information
P.O. Box 62
Oak Ridge, TN 37831

Telephone: (865)576-8401
Facsimile: (865)576-5728
E-Mail: reports@adonis.osti.gov
Online ordering: http://www.doe.gov/bridge

Available to the public from
U.S. Department of Commerce
National Technical Information Service
5285 Port Royal Rd
Springfield, VA 22161

Telephone: (800)553-6847
Facsimile: (703)605-6900
E-Mail: orders@ntis.fedworld.gov
Online order: http://www.ntis.gov/help/ordermethods.asp?loc=7-4-0#online

SAND2002-8592
Unlimited Release
Printed December 20002

Small-Scale Multiaxial Deformation Experiments on Solder for High-Fidelity Model Development

Wei-Yang Lu and T. Jesse Lim
Microsystems and Materials Mechanics Department
Sandia National Laboratories
Livermore, CA 94551-0969

Brad L. Boyce
Microsystem Materials, Tribology and Technology Department

J. Mark Grazier
Joining and Coating Department

H. Eliot Fang
Materials and Process Modeling Department
Sandia National Laboratories
Albuquerque, NM 87185-1081

Abstract

Solder in our applications is used for more than just an electrical connection. It also serves as the load bearing structures for some electronic components. Thus the mechanical properties of solder interconnects were studied to ensure the reliability of electronic assemblies. Studies include deformation and failure associated with size effect, deformation mechanism map, and microstructural coarsening. Results show that tensile stress-strain behavior is size dependent. Small solder specimens do not follow bulk material properties when the cross-sectional area of the gage section is less than 0.1 mm^2. The effect of microstructural size is found to be minimal, based on two averaged Pb-rich phase sizes, 2 and 4 μm. From multiaxial creep experiments at room temperature and 100^oC, the activation energy and stress exponent are consistent with published values for Region-I creep behavior. The creep conditions explored in this study establish the aspects of a multiaxial deformation mechanism map that are typical of normal stockpile conditions. The Von Mises equivalent stress appears to work well for various loading modes. The coarsening phenomenon of eutectic solder is still not very clear. It requires a large number of observations to mitigate the extensive variability in both starting microstructure and response. From isothermal torsional fatigue at 10^{-4} and 10^{-5} s^{-1}, there is no correlation between the initial phase size and the magnitude of accumulated strain experienced by the specimen. In creep specimens, localized coarsening is observed at the failed region for some loading conditions, predominantly under pure shear.

ACKNOWLEDGEMENT

Many thanks to P. Vianco and B. Antoun for insightful suggestions and review of this manuscript. Thanks also to N. Yang for technical discussions, T. Buchheit, D.T. Schmale and D. LaVan for multiaxial creep frame design and fabrication, J. Mayer for preliminary multiaxial creep evaluation, J. Korellis for fatigue experimental setup, J. Rejent for assisting in creep specimen fabrication, as well as J. Chames, J. Yio, B. McKenzie and R. Grant for scanning electron microscope (SEM) characterization. Sandia is a multiprogram laboratory operated by Sandia Corporation, a Lockheed Martin Company, for the United States Department of Energy under contract DE-AC04-94AL85000.

TABLE OF CONTENTS

1. Introduction

This report documents results and findings made during a three-year LDRD (Laboratory Directed Research and Development) investigation of 37Pb-63Sn solder, which focuses on understanding the underpinning mechanisms of its deformation and failure.

Solder has been used in electronic packaging for decades. Over the years, the size of a solder joint has become smaller and smaller. For example, the diameter of a traditional pin through hole (PTH) solder joint, which is contained in 90% of the stockpile, is about 2 mm. The solder size of a more advanced surface mount technology (SMT) is about 0.5 mm, which accounts for approximately 10% of the solder joints in the existing stockpile. For modern Ball Grid Array (BGA) and Chip Scale Package (CSP) technologies used in semiconductor industries, the size of solder bumps is on the order of 0.1 mm.

Solder in our applications is used for more than just an electrical connection. For SMT and newer technologies, solder interconnects also serve as the load bearing structures that hold the electronic component and the printed wiring board (PWB) together. Thus it is important to study the mechanical properties of solder interconnects in order to ensure the reliability of electronic assemblies. Since the use of drop-in replacements for Lead-Tin (PbSn) solder (Lead free solder, conductive adhesives) has not been adopted, PbSn solder will remain as the primary material for electrical interconnects.

Solder is a two-phase alloy and has a low melting point, T_m = 183^{o}C (456^{o}K), so room temperature (about 0.65 T_m) is a high homologous temperature. Therefore, the microstructure is constantly changing even at room temperature. The ambient temperature deformation of solder is complicated by competing, thermally activated mechanisms. Electronic assemblies have a service life of up to 40 years in typical weapon stockpile. Degradation and failure of soldered interconnects poses a significant reliability concern for electronics assemblies in the stockpile .

It has been identified that thermomechanical fatigue (TMF) is one prominent degradation mechanism for solder interconnects in the stockpile. Environmental temperature changes and thermal expansion mismatch between the PWB and the ceramic chip carrier causes cyclic strain in solder joints. The solder joint deforms heterogeneously and the maximum strain could reach 20% during TMF. It has long been recognized that coarsening of Pb-rich phase particles will occur during TMF of 63Sn-37Pb eutectic solder and eventually cracks will form in these coarsened regions resulting in mechanical and electrical failure [1,2]; however, the mechanism of microstructural evolution with deformation under various temperature and stress conditions is not thoroughly understood. Meaningful experimental data must be carefully collected to understand and separate the interplay between various deformation mechanisms.

This experimental investigation addresses the following three issues, identified by the Accelerated Strategic Computing Initiative (ASCI) solder TMF project, and tries to validate assumptions and elucidate underpinning mechanisms used in computational models.

The first issue is the size effect. Experimental and simulation results have demonstrated that samples with less than 10 grains through the cross-section behave in a different manner than classic continuum polycrystals. In a classic polycrystal, composed of an endless sea of thousands or more grains, the deviation of a single grain is negligible in the overall response. Devices with few grains through a critical dimension behave differently because of the reduced constraint imposed on each grain and the increased significance of each grain's contribution. Current continuum- and microstructural-based models are able to reproduce the effect of reduced constraint, but the physical phenomena are not isolated in bulk mechanical property experiments. As joint size decreases, solder response will change from classic polycrystalline behavior to a scale where bulk, size independent constitutive relations no longer hold, and model accuracy will degrade unless the models are adjusted to account for this non-continuum behavior.

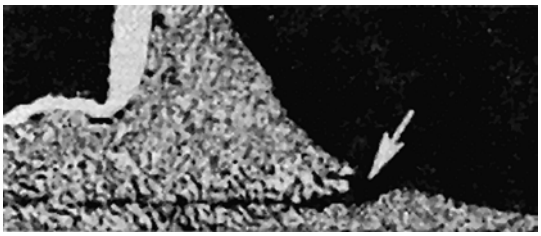

Figure 1.1. Example of a failed surface mount solder joint.

The second issue is deformation mechanisms under multiaxial conditions, e.g., combined tension and shear stress state. Developing and applying the correct constitutive relations in finite element simulations becomes impossible without knowing which deformation behaviors to model under various stress-temperature conditions for solder with a given microstructure. Large-scale simulations can incorporate detailed deformation mechanism maps that define which microstructural mechanisms are operative across stress, temperature, microstructural size, and strain rate space. Unfortunately, a complete and detailed deformation mechanism map does not exist for solder. The data available in the literature was not produced using standardized techniques or controlled microstructures, nor were the effects of stress state well established.

The third issue is localization and microstructural coarsening, showing the Pb-rich phase size grows larger. Failed devices, Figure 1.1 [1], often show localized microstructural coarsening at or near the point of failure in Pb-Sn solder. Test specimens loaded axially have shown uniform coarsening; localized coarsening is only observed in samples subjected to shear. The effect of coarsening on solder joints failure is not clear. Current microstructural evolution models incorporate a scalar term derived from plastic strain energy to drive coarsening [3]. These models do not consider elastic strain energy or contributions from hydrostatic stress. They also do not account for the interaction between hydrostatic stress, void nucleation and growth, and microstructural coarsening.

2. Size Effect

2.1. Introduction

The size-scales of both the specimen diameter and the microstructure (Pb-rich phase size) were intentionally varied in this study. Specimen diameters were varied over the range of 6 mm to 0.084 mm, and three length-to-diameter aspect ratios, 1, 3, and 7 (or larger), were evaluated. Microstructural size scale was varied at two levels of Pb-rich phase size, 2 and 4 μm, as established by aging at 100°C for either 16 hours or 25 days. Monotonic tension and torsion experiments were used to evaluate the role of specimen and microstructural size scales on deformation behavior.

2.2. Specimen Preparation

The PbSn alloy used was a 37Pb-63Sn eutectic solder alloy supplied by Kester Solder. Three methods were used to fabricate specimens, depending on the size scale of the specimen. The first method was used to fabricate specimens typically larger than 1.0 mm in diameter. A steel or aluminum mold was fabricated with a cylindrical cavity. Two brass rods of the same diameter as the cylindrical cavity, were clamped at both ends of the mold to be used as grips for the intermediate solder joint. The whole assembly was heated to ~200°C, and molten PbSn was flowed into the mold. After molten PbSn filled the mold, the assembly was quickly quenched in water, thereby solidifying the solder between the two brass grips. After the solder perform and adjoining brass ends were removed from the mold, the gage section was machined to a precise dimension as shown in Figure 2.1(a). The specimen was subsequently aged to obtain the desired microstructure. The aging treatments are described in the following section.

Deleted: <sp><sp><sp>

The second fabrication method was used to produce specimens less than 1.0 mm in diameter, where machining is no longer practical. The mold was machined with the shape of the gage section, Figure 2.1(b). Following the same procedure of filling mold with molten solder, quenching the assembly in water, and removing the specimen from mold as the same as the first method, the specimen was ready for aging treatment. Unfortunately, air bubbles

(a) (b)

Figure 2.1. (a) The specimen with a straight section in between two brass ends as cast, the PbSn gage section was machined; (b) the mold for making PbSn specimens with the gage section machined in the mold;

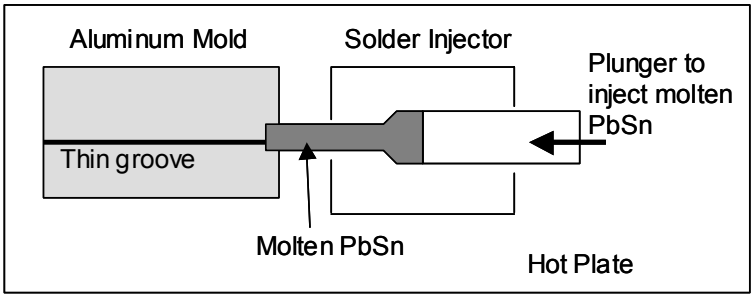

Figure 2.2. Setup to fabricate small ribbon type specimens.

were sometimes entrapped in the mold, which resulted in voids on the surface of the gage section. Those specimens were not useable. Specimens were carefully screened before testing.

The third method was used to produce specimens with a thickness less than 0.1 mm. A block of aluminum was machined to have a thin and shallow groove, about 0.25 mm wide and 0.1 mm thick. It was then clamped on top with another flat piece of aluminum. The assembly was then place on top of a hot plate with the "solder injector" attached, Figure 2.2. Molten solder was then injected into the mold and the ribbon type specimen was made. After quenching, the ribbon was removed from the mold. Similar to the second method, voids were common. Void-free sections were extracted from the wire for subsequent aging and evaluation.

2.3. Aging Treatment

Two different aging treatments were applied after rapid solidification. The first treatment was 100°C, atmospheric air for 16 hours (hereafter refer to as 16H aging), which

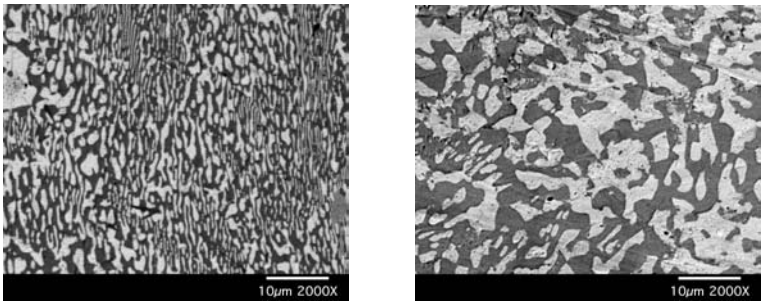

(a) (b)

Figure 2.3. (a) SEM backscatter image of the surface of a 100°C, 16 hours aged specimen, (b) SEM backscatter image of a 100°C, 25 day aged specimen.

typically resulted in an average Pb-rich phase size of about 2.0 μm. The second was 100°C, atmospheric air for 25 days (hereafter refer to as 25D aging) which typically resulted in an average Pb-rich phase size of ~4.0 μm. Figure 2.3 shows the scanning electron microscope (SEM) backscattered images of microstructures from these two treatments. The light colored regions are Pb-rich phase while the dark colored matrix is the Sn-rich phase.

2.4. Tensile Experiment

The cylindrical specimens were characterized by two parameters, the gage length (L) and the diameter (ϕ or D); The specimen aspect ratio AR, was defined by AR=L/ϕ. In Table 2.1, monotonic tension tests of specific aging treatment, specimen size and aspect ratio with an "x" mark were performed. In all experiments, the average tensile strain rate was $10^{-4}s^{-1}$, and specimens were strained until failure. Each case was repeated at least three times to establish reproducibility.

Tension experiments for specimens with diameter equal or less than 1.0 mm were performed on a MTS Tytron Microforce System, shown in Figure 2.4. The system has a load capacity of 250 N with load and displacement resolutions of 0.1 mN and 0.1 μm, respectively. Such high resolution is required for such small solder specimens. For specimen diameter larger than 1.0 mm, tests were performed using a MTS Minibionix Biaxial System with a larger force capacity. Tytron and Minibionix systems are computer controlled using TestStar IIs and IIm, respectively. Both are capable of automatic data acquisition and monotonic or cyclic loading with a user programmed rate and magnitude.

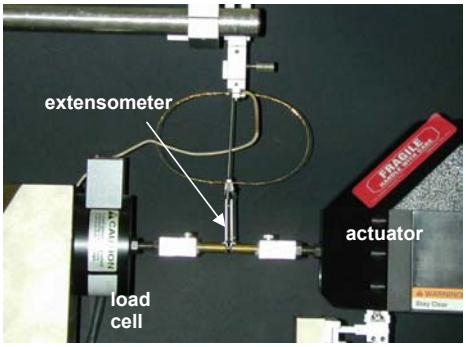

Figure 2.4. Tensile experimental setup based on MTS Tytron Microforce System.

Table 2.1. Experimental matrix for monotonic uniaxial loading

Aging	Dimension, mm (Area, mm^2)	2.20 D (3.80)	1.0 D (0.78)	0.35 D (0.096)	≈ 0.25 x 0.1* (0.025)
16H	AR = 1	x	x	x	
16H	AR = 3	x	x		
16H	AR ≥ 7		x	x	x
25D	AR = 1	x	x	x	
25D	AR = 3		x		
25D	AR ≥ 7		x	x	x

* small ribbon type specimen with a rectangular cross section.

Some post-test tensile specimens are shown in Figure 2.5. Typical experimental results of engineering stress-strain curves are shown in Figure 2.6, for two cases: (a) 16H, AR=7, 0.25x0.1 mm, and (b) 25D, AR=7, ϕ=0.35 mm, respectively. The engineering stress-strain curve of each specimen, represented by a distinctive color in the figure, showed a well-defined ultimate strength followed by strain softening. In general, the ultimate strength scatter was within ±4 MPa for the worst case and the failure strain varied in a wide range from 0.4 to over 1.

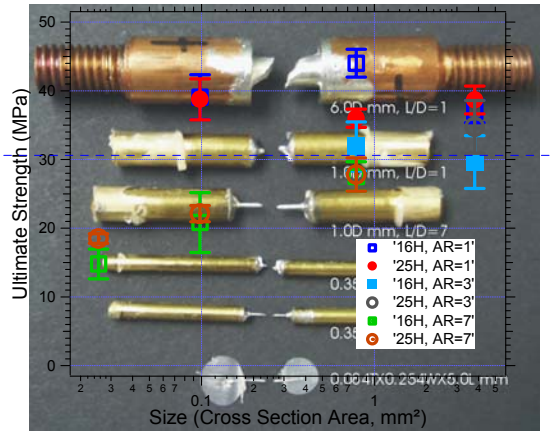

Figure 2.7. Ultimate strength plotted against specimen size.

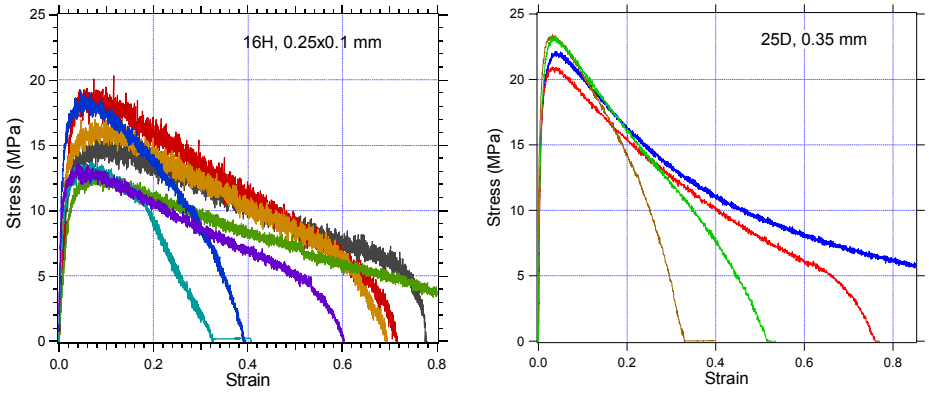

(a) (b)

The average ultimate strength versus the specimen size is plotted in Figure 2.7. In the figure, the error bar indicates one standard deviation of the ultimate strength of all the specimens tested for the particular parameters (heat treatment, specimen aspect ratio and size). It is apparent that for a low AR (AR=1), the ultimate strength is higher. As the AR becomes higher (AR>3), the ultimate strength decreases, and it is approaching a constant regardless of the AR. This is consistent with the finite element analysis discussed in the following paragraph. As for high AR specimens, the flow stress immediately after yielding is comparable to the strain-rate jump test as performed by Whitelaw et. al. [4] on 60Sn-40Pb alloys. Another observation is that for high AR specimens, the ultimate strength decreases as the size decreases. This size effect and deformation mechanism of small size specimens (<0.1 mm^2) will be discussed later in this section. In general, experimental results do not

show the effect of Pb-rich phase size on the ultimate strength. With the exception of the 1mm, AR=1 specimens, 16H and 25D aging treatments resulted in similar ultimate strengths.

Finite element analysis (FEA) was employed to understand the detailed mechanics in the gage section of the PbSn solder specimen. A PbSn specimen was modeled in quarter symmetry with axisymmetric elements as provided by ABAQUS, shown in Figure 2.8. Two different specimen diameters ϕ = 2.2 and 0.35 mm, and four aspect ratios, AR = 0.5, 1, 3, and 7, were modeled.

In the FEA model, all bottom nodes were constrained in the axial direction and the leftmost nodes were constrained in the radial direction to model the quarter symmetry. The nodes at the far end of the brass (top nodes) were then given a ramp function such that the average strain rate at the gage section was 10^{-4} s^{-1}. It was assumed that both the brass and PbSn alloy have continuous and isotropic properties. The Young's modulus of brass was taken to be 110 GPa with a Poisson's ratio of 0.34. For PbSn alloy, the Young's modulus was taken to be 15GPa with a Poisson's ratio of 0.43. It was also assumed that the PbSn alloy deforms perfectly plastic with a flow stress = 30 MPa at a strain rate of 10^{-4} s^{-1} that increases to 54 MPa at a higher strain rate of $10^{-3}s^{-1}$. The FEA simulations of the stress-strain behavior of 2.2 mm diameter specimen with various aspect ratios are shown in Figure 2.9. Although the modeling showed the general trend that the ultimate strength increases as the AR decreases, the ultimate strength of the AR=1 specimen doesn't approach the level observed experimentally. Only as AR goes down to 0.5, does the ultimate strength of FEA simulations approach the actual experimental value of specimens with AR=1.

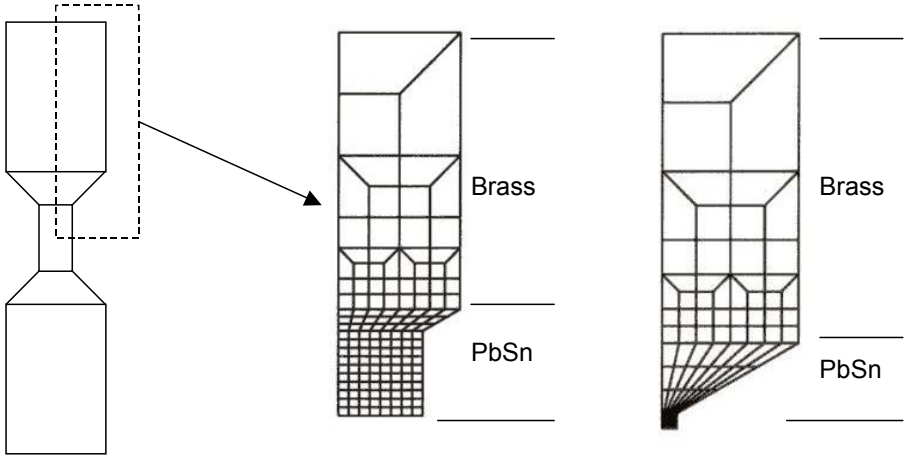

Figure 2.8. A quarter symmetry of the Specimen was modeled in finite element analysis using ABAQUS.

Finite element analysis offers additional insight into the experiments. Figure 2.10 shows the contour plots of strain rates in the strain softening region. The average strain rate is 10^{-4} s^{-1}; however, for a more constrained gage section (low AR), the material near the constraint (the end of the gage section) has a lower strain rate and the less constrained material has a higher strain rate. For a high AR specimen, since most of the material in the gage section is free of constraint, most of the material has a uniform strain rate near 10^{-4} s^{-1}. Since the flow stress of PbSn alloy is rate sensitive, the Von Mises stress in high strain rate areas is higher as shown in the contour plot of Figure 2.11. As a result, the average axial stress increases with increasing constraint.

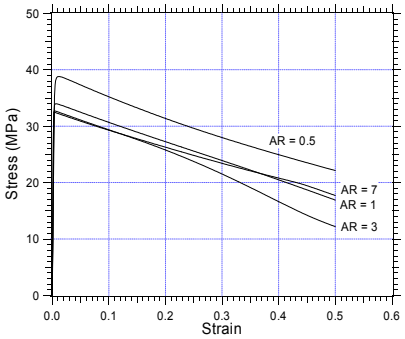

Figure 2.9. FEA predicted engineering stress-strain response of ϕ=2.2mm specimens.

.

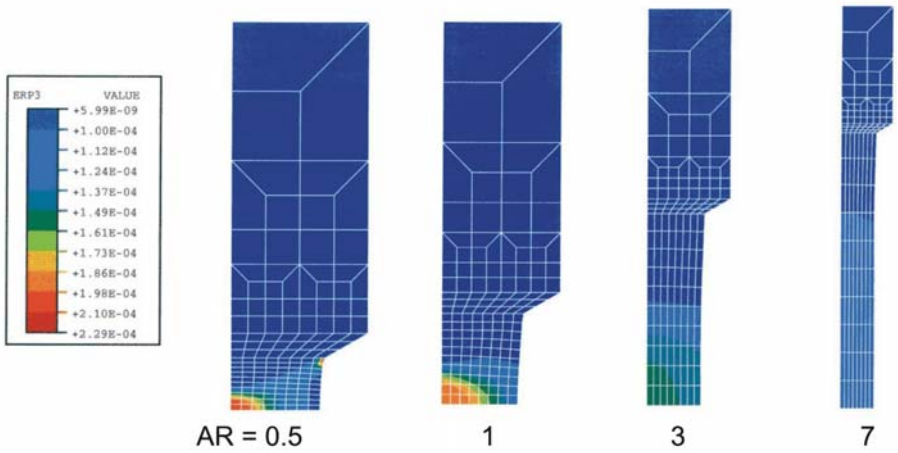

Figure 2.10. Principle strain rate distribution for specimens of various specimen aspect ratios obtained from finite element analysis.

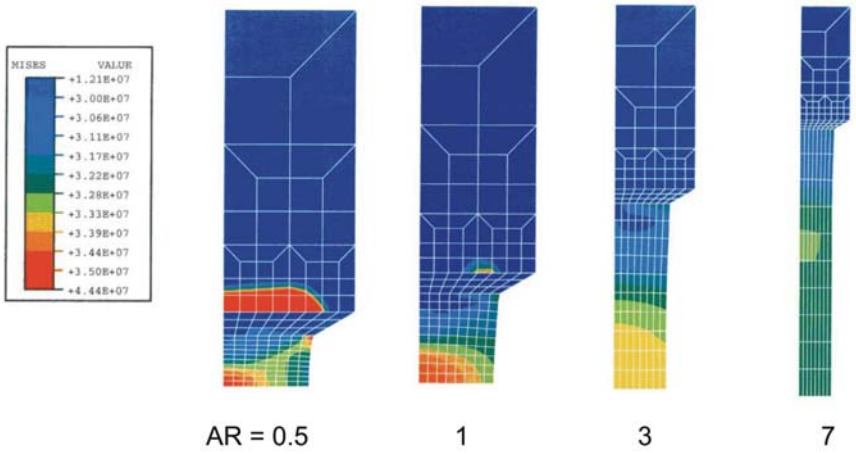

Figure 2.11. Von Mises stress distribution for specimens of various specimen aspect ratios obtained from finite element analysis.

Without size effect built into the finite element model, the predicted ultimate strengths for specimens with the same aspect ratio are essentially the same regardless of their diameter, as shown in Figure 2.12. This is in contrast to the experimental observations as reported in Figure 2.6, where the ultimate strength of the smallest specimens is much lower than the larger specimens. Microstructural analysis was conducted to study the deformation of the thin specimens.

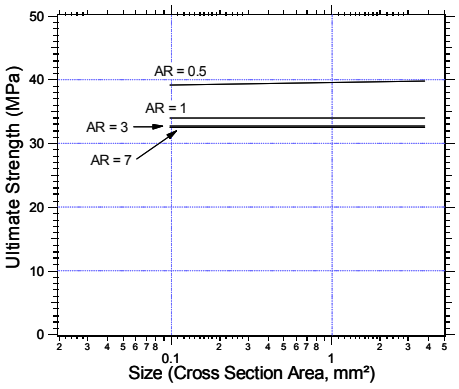

Figure 2.12. Ultimate strengths solder specimens predicted from finite element analysis.

The smallest solder specimen, with a cross-section of was 84x254 μm, exhibited an ultimate tensile strength of 17.0 MPa and a maximum engineering strain of 0.7. The post-test specimen is shown on the bottom of Figure 2.5. The SEM image of one half of the broken specimen is displayed in Figure 2.13, showing multiple necked regions in the gage section. This phenomenon was not observed for $\phi \geq 0.35$ mm specimens.

Figures 2.14 and 2.15(a) show SEM micrographs of another thin solder specimen before and after deformation, respectively. The cross-sectional dimensions of the specimen were 1.0x0.08 mm, and the average axial strain was about 20%. Originally straight edges and smooth surfaces of the specimen became curved and rough after deformation. Clearly the deformation was not uniform, and it concentrated on cell boundaries between regions of uniform crystallographic orientation. Figures 2.15(a) and (b) illustrate cell boundaries, showing approximately two or three cells through the thickness. These observations indicate possible boundary sliding or rotation during loading.

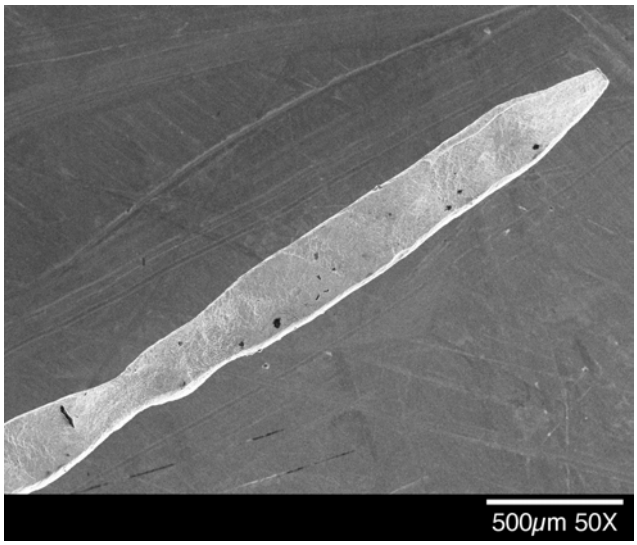

Figure 2.13. Multiple necks on a thin tensile specimen.

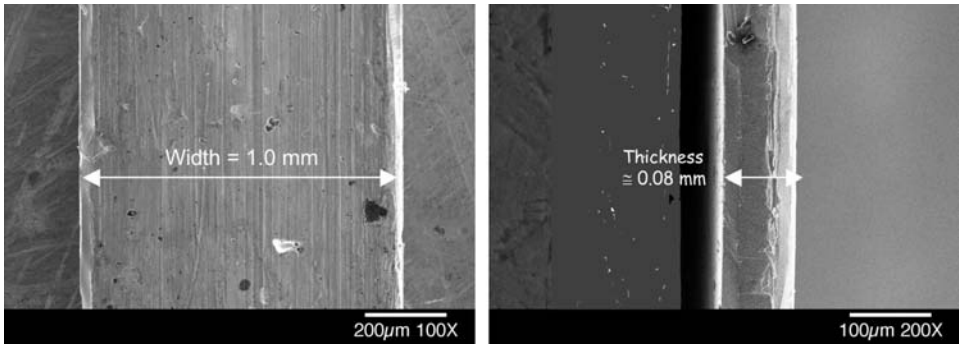

Figure 2.14. SEM micrographs of an undeformed thin solder specimen.

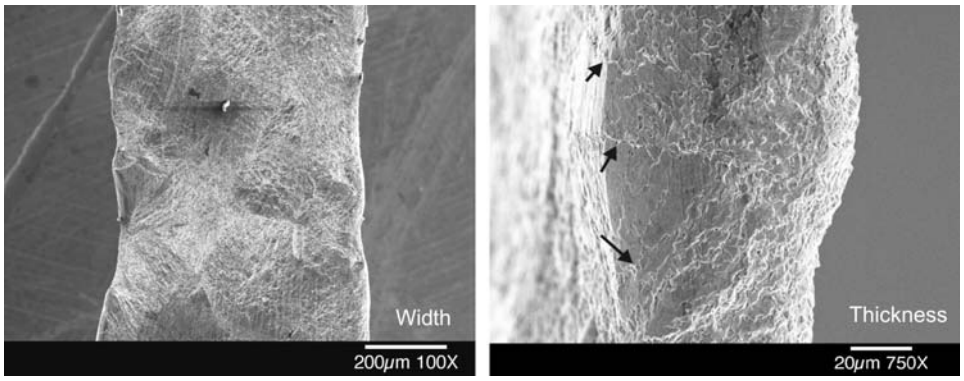

(a)

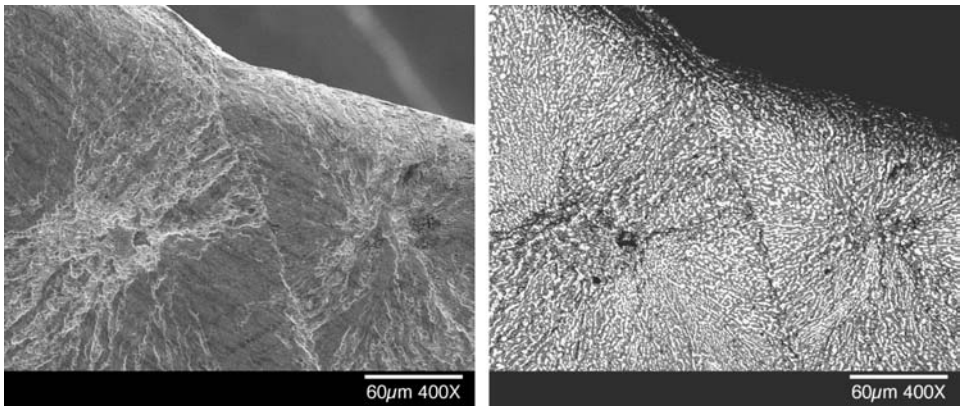

(b)

Figure 2.15. (a) SEM micrographs of a deformed thin solder specimen. (b) SEM secondary (left) and backscatter (right) images of the deformation at a cell boundary.

2.4. Monotonic torsional loading

All torsional experiments were performed using the MTS Torsion Master System, shown in Figure 2.16. The system is capable of continuous rotations and the torque resolution is better than 100 μN-m. TestWork 4 is the control software of the system.

Specimens with AR=1 were prepared. It was assumed that in shear, the change in AR would not alter the state of constraint of the materials in the gage section, so specimens of other AR values were not made. In addition to solid specimens, thin walled tubular specimens were also prepared by boring through the axis of the solid specimens. The ratio of the thickness to outer diameter was 0.1. Referring to Table 2.2, specimens with two different diameters, 2.54mm and 5.08mm, as well as both solid and thin walled tubular specimens, were prepared and tested. Some post-test specimens are shown in Figure 2.17.

Table 2.2. Test matrix for monotonic torsional loading.

Diameter (mm)	2.54	5.08
Solid	x	x
This walled tube	x	x

Figure 2.18 shows the typical equivalent stress-strain curve of the respective specimens. Both the equivalent strain, ε_{eq}, and equivalent stress, σ_{eq}, were evaluated at the specimen surface with relation to shear stress and strain as:

$$\varepsilon_{eq} = \gamma / \sqrt{3} \quad \text{and} \quad \sigma_{eq} = \sqrt{3}\tau\,, \tag{2.1}$$

where γ is the engineering shear strain and τ is the engineering shear stress. In torsion, the ultimate strength is comparable to that of uniaxial tension. However, the failure strain can be

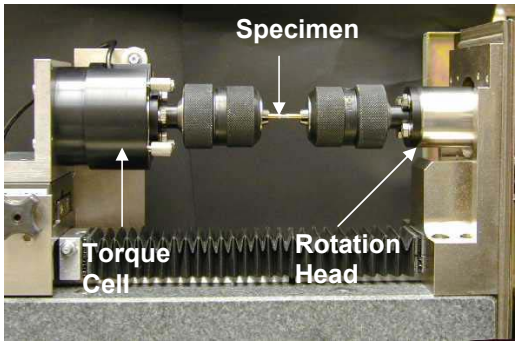

Figure 2.16. MTS TorsionMaster System

Figure 2.17. Post-experiment torsion specimens.

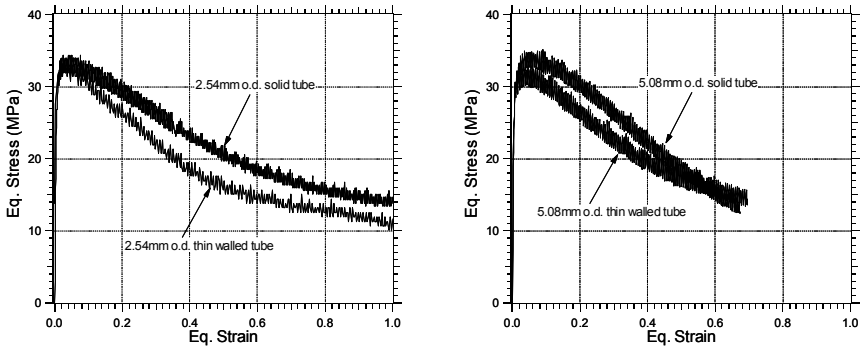

Figure 2.18. Typical equivalent stress-strain curves of solid or thin walled tube specimens.

well over 1. The initial deformation of a torsional specimen is uniform. As the loading proceeds, localization occurs within the gage section. Different from tensile loading, the material in the localized section simply rotates perpendicular to the axis of rotation without any reduction in cross sectional area, which results in large shear strain without failure. This phenomenon was observed in Figure 2.19. Horizontal lines were drawn on the specimen before the experiment, so the deformation at the gage section was indicated by the lines. In Figure 2.19(a), deformation localization had just begun to form at the region marked by an arrow. Figure 2.19(b) shows that large rotation was concentrated in the dotted area.

In the torsional loading experiments, there was no observable size and stress gradient effect. The torsional specimens had essentially identical bulk dimensions to that of the uniaxial tension specimens. The smallest dimension in the torsion specimens was the thickness of the thin-wall tube, t = 0.254 mm. Smaller scale specimens may have demonstrated a size or stress gradient effect, but such experiments were not possible with the existing torque cell resolution.

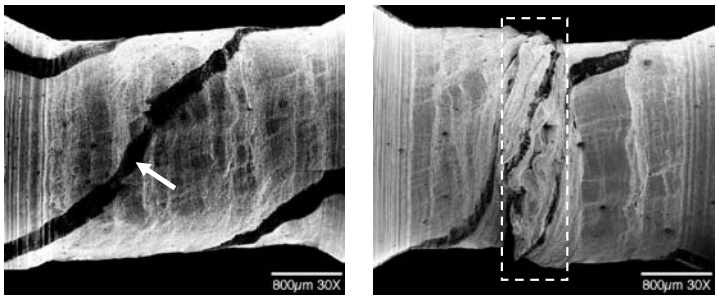

Figure 2.19. Localization of deformation in torsional loading does not reduce cross sectional area and results in large shear strain without failure.

2.5. Summary of Size Effect

Under tensile loading, the specimen length-to-diameter aspect ratio was found to affect the apparent engineering stress-strain curve. Specimens with a low aspect ratio, <3, have a complex triaxial stress state in the gage section and result in a higher ultimate strength. When the aspect ratio is greater than 3, the stress state approaches uniaxial and is uniform in the gage section. For torsional loading, the aspect ratio of cylindrical or tubular specimens was observed to have no effect on ultimate strength.

Experimental results indicated that the ultimate strength was lower for specimens with a cross-sectional area smaller than 0.1 mm^2. The deformation was nonuniform, highly concentrated on cell boundaries, and multiple necks were formed a behavior not observed in larger specimens. For torsional experiments, there was no observable effect of specimen size.

Pb-rich phase sizes of 2.0 and 4.0 μm were not found to result in significant differences in stress-strain response.

3. Cyclic Loading

3.1. Introduction

Cyclic loading experiments were conducted to investigate the fatigue properties of solder. Most experiments were isothermal fatigue at room temperature and 100°F, including both axial (tension-compression) and torsional fatigue loading. Limited thermal cycling experiments were also performed. The investigation was focused on microstructural coarsening and damage evolution.

The experimental setup for isothermal fatigue was the same as that for monotonic loading. Tytron and Torsion Master systems, Figures 2.4 and 2.16, were used for axial and torsional fatigue, respectively. Equivalent strain rates were kept constant at 10^{-4} s^{-1}, identical to that of the monotonic loading experiments. In fatigue tests, only one specimen size, ϕ=1.0mm and AR=3, was used for axial fatigue, and one specimen size, ϕ=2.54mm and AR=1, for torsional fatigue. These specimens provided simple stress states and had bulk deformation behavior. Both 16H and 25D aging specimens were considered in torsional fatigue to study the effect of Pb-rich size on fatigue.

3.2. Fatigue Life

Typical stress-strain responses of tension-compression fatigue at room temperature with strain ranges ±0.5% and ±1.0% are shown in Figures 3.1(a) and (b) , respectively. Torsional fatigue stress-strain hysteresis is shown in the following section.

As strain-controlled cycling proceeds, the stress amplitude decreases as fatigue damage accumulates in the specimens. The fatigue life, N_f, was defined as the number of cycles, N, in which the stress level drops by 50% from the initial stress level at N=1. The strain-life of all specimens is displayed in Figure 3.2. Polished surfaces were observed to

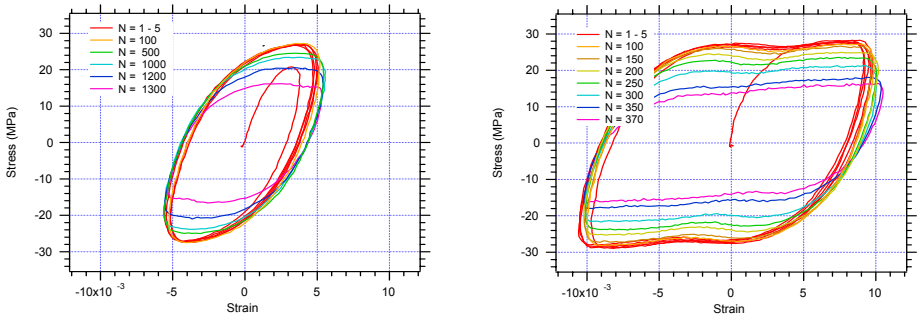

(a) (b)

Figure 3.1. Typical stress strain curves as cycling proceeds for uniaxial tension specimens: (a) –0.5%<ε<0.5%, and (b) –1.0%<ε<1.0%.

result in somewhat longer lives, as was observed for the 16H aging treatment in torsion. The observed fatigue life in uniaxial tension-compression tests was comparable to that reported by Jiang et al. [5] at a strain rate of $3.33 \times 10^{-3} s^{-1}$.

Comparing the results of 16H and 25D polished torsional specimens, the 25D specimens exhibited a longer fatigue life, consistent with the published qualitative observation that fatigue life increases with the length of aging treatment [6,7].

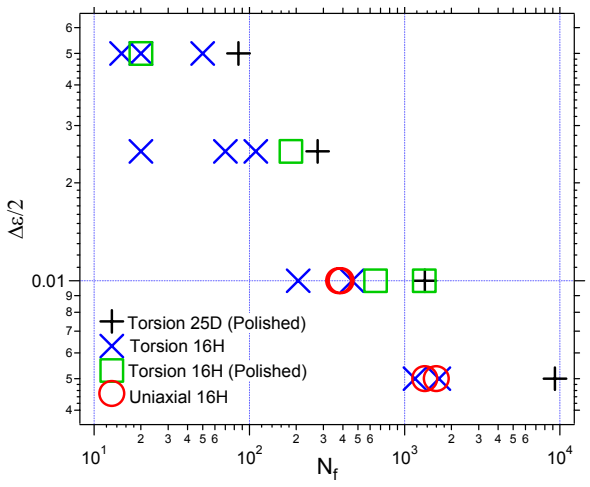

Figure 3.2 Strain-life points for specimens of different type.

The specimen surface of the 1% equivalent strain specimens of both uniaxial and torsional fatigue were examined using scanning electron microscopy (SEM), Figures 3.3(a) and (b), respectively. Fatigue cracks had developed along the phase boundary between Pb-rich phase and Sn-rich phase, and in some case, within the Sn-rich phase and Pb-rich Phase. These micro-cracks eventually coalesce into large cracks, Figures 3.3(c) and (d), culminating in specimen failure. The fatigue damage mechanisms appeared similar for both tension-compression cycling and torsional cycling, and the fatigue lives for both types of loading were also similar as indicated in Figure 3.2. This observation is consistent with published literature; however, further experiments with non-proportional loading should be carried out since such a loading mode is expected to decrease the fatigue life [8].

3.3. Damage and Coarsening During Isothermal Fatigue

It is known that microstructural coarsening occurs during TMF, which involve both mechanical deformation and time at temperature. The solder microstructure is constantly evolving at room temperature, and the rate of coarsening by TMF is appreciably greater than that by isothermal aging alone [9]. It is unclear whether coarsening can be separated into independent mechanical and thermal terms or if strain has to be coupled with temperature to activate various deformation mechanisms and trigger coarsening [10]? To study this strain enhanced coarsening during fatigue, 16H aged torsional fatigue specimens were used.

During torsion, cylindrical specimens experience no strain at the center and a maximum strain the outer surface. If the average phase size of Pb-rich phase is uniform throughout the entire specimen before deformation and the strain-enhanced coarsening

occurs at constant temperature, then after loading, the Pb-rich phase at the circumference of the specimen would be expected to be larger then that at the center.

One as-received, or undeformed, specimen and four room temperature fatigue-fractured torsional specimens were cross-sectioned and SEM images were taken for microstructure analysis. A typical set of images is shown in Figure 3.4.

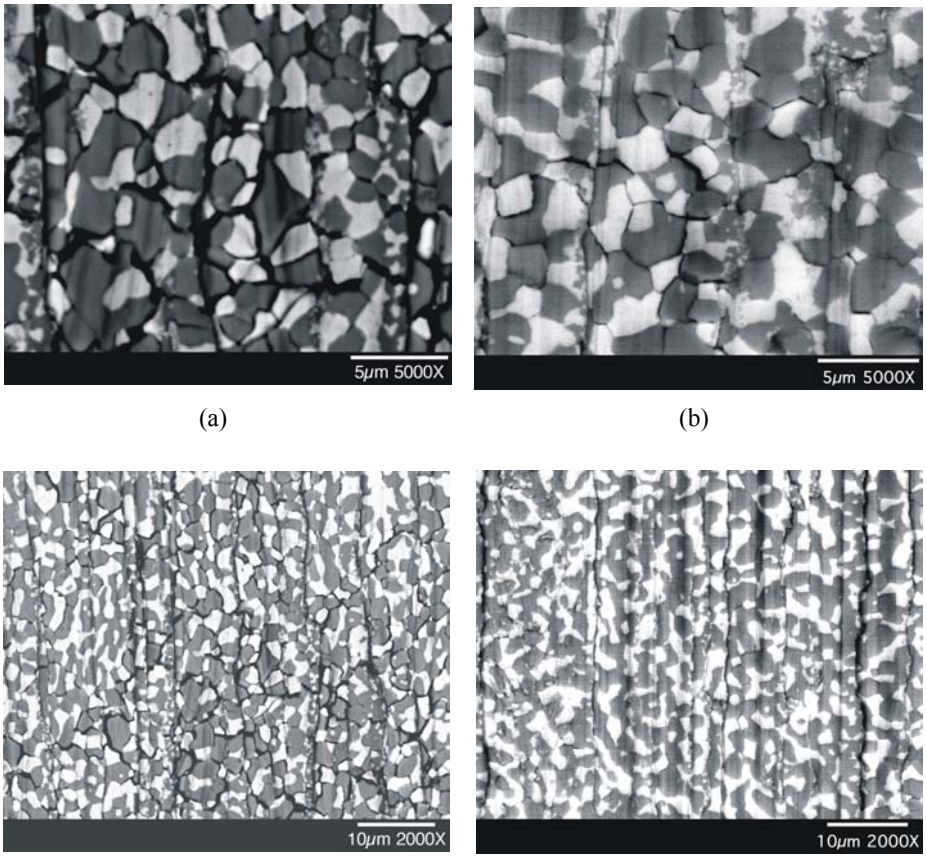

Figure 3.3. SEM backscatter images of fatigue damaged specimens with ±1% equivalent strain amplitude, showing the microcracks along the inter-phase boundary or with the Sn-rich phase or Pb-rich phase: (a) tension-compression, and (b) torsion; and large cracks: (c) tension-compression, and (d) torsion.

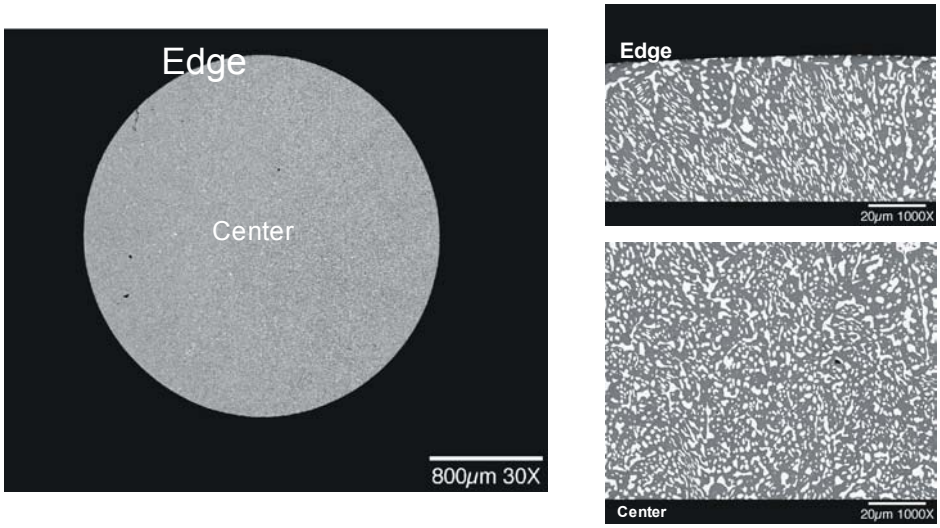

Figure 3.4. Different places on the cross-section of the fatigued specimen were taken and the phase sizes measured.

The phase sizes at the edge and the center were then measured using the image processing software *Image Pro Plus* [11]. Table 3.1 summarizes the Pb-rich phase sizes as measured at the two locations, center and edge, for the four strain amplitudes. Notice that the phase size is given in both area size (μm^2) and linear size (μm). Image Pro Plus software measures the phase sizes in area, and the linear size is calculated by $D=2(A/\pi)^{0.5}$, where D is the linear size and A is the average area size of the Pb-rich phases as measured.

Table 3.1. Pb-rich Phase sizes of torsional fatigue specimens.

Specimen	Average Pb-rich Particle Size			
	Center (μm^2)	Center (μm)	Edge (μm^2)	Edge (μm)
As received	6.94	2.97	2.49	1.78
Fatigued, $\varepsilon_{eq} = \pm 0.5\%$	1.98	1.59	2.31	1.71
Fatigued, $\varepsilon_{eq} = \pm 1.0\%$	4.50	2.39	4.70	2.45
Fatigued, $\varepsilon_{eq} = \pm 2.5\%$	2.38	1.74	2.47	1.77
Fatigued, $\varepsilon_{eq} = \pm 5.0\%$	1.66	1.45	1.93	1.57

From Table 3.1, it appears that the Pb-rich phase size at the edge is slightly larger than that at the center for fatigued specimens, but there seems to have no correlation between the initial phase size to the magnitude of accumulated strain experienced by the specimen. Moreover, for the as-received specimen, the phase size is not consistent and varies from center to edge. Together with the inconsistency of phase sizes among different specimens, it is difficult to draw a definite conclusion about the strain-enhanced coarsening.

To better study the coupled phase coarsening and fatigue effects, a different procedure was developed. The idea was to keep track of the size of Pb-rich phase at one specific spot on the specimen surface throughout the fatigue loading. In this study, torsional specimens with 16H aging were again used. Since in-situ fatigue loading and observation of the microstructure under scanning electron microscope (SEM) was not available, a fatigue test was interrupted several times to measure the Pb-rich phase size at exactly the same location. In each specimen, physical markings were made by either a scratch mark with a knife or a spot of carbon paint as shown in Figure 3.5. Before any loading, SEM pictures were taken. Specific coordinates, as shown in the xy-translation stage of the SEM, of the physical markings and hence any spot on the specimen were recorded. The specimen was then subjected to fatigue cycles. The specimen was then reloaded into the SEM, and returned to the exact same location, allowing comparison of the microstructure at the spot before and after load cycling, and recording of images for analysis.

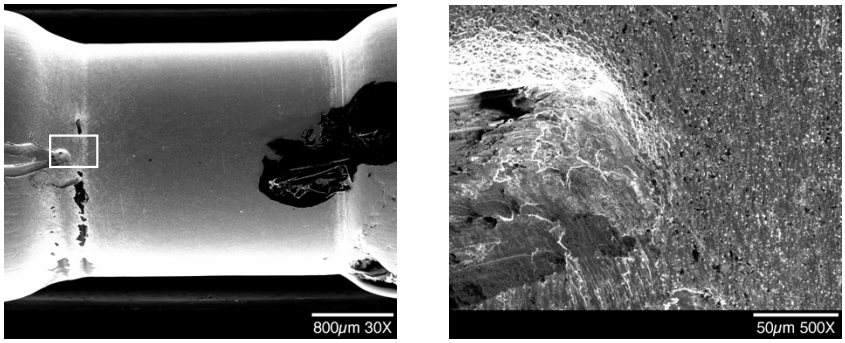

Figure 3.5. The torsional specimen is shown on the left, the knife mark as highlighted can be tracked as indicated on the right and the coordinates recorded.

The test matrix is shown in Table 3.2. Specimens 6100 and 6104 experienced no load cycling at all; they served only as baseline measure of thermally-induced phase growth, hence they were designated as "Idle". Each loading set for specimens 6101 to 6103 and 6105 to 6107 was either ±1.0% for 25 cycles, ±2.5% for 10 cycles or ±5.0% for 5 cycles at an equivalent strain rate of $10^{-4}s^{-1}$. These were chosen to ensure all the specimens experienced the same cumulative strain. In the case of high temperature specimens, each specimen would experience the same time period of exposure at temperature. The three values for maximum equivalent strain were chosen to investigate the effect of maximum strain on fatigue life and

phase growth. In between each loading set and before any loading, the microstructure was documented in the SEM, so the change in microstructure could be correlated to the load cycling and thermal effects. For each specimen, multiple locations were tracked.

Table 3.2. Test matrix for isothermal fatigue and strain-enhanced coarsening study.

		Room Temperature				Temperature = 100°C			
	Specimen	6100	6101	6102	6103	6104	6105	6106	6017
Step	Eq. Strain, %	0	±0.01	±0.025	±0.05	0	±0.01	±0.025	±0.05
1		SEM	SEM	SEM	SEM	SEM	SEM	SEM	SEM
2	Loading Set 1	Idle	N=25	N=10	N=5	Idle	N=25	N=10	N=5
3		SEM	SEM	SEM	SEM	SEM	SEM	SEM	SEM
4	Loading Set 2	Idle	N=25	N=10	N=5	Idle	N=25	N=10	N=5
5		SEM	SEM	SEM	SEM	SEM	SEM	SEM	SEM
6	Loading Set 3, 4	Idle	N=50	N=20	N=10	Idle	N=50	N=20	N=10
7		SEM	SEM	SEM	SEM	SEM	SEM	SEM	SEM

The cyclic stress-strain responses of room temperature specimens, 6101 to 6103, are shown in Figures 3.6(a) to (c), respectively. As expected, the higher the maximum strain, the faster the damage accumulates. The stress-strain responses of high temperature specimens, 6105 to 6107, are shown in Figures 3.7(a) to (c), respectively. At high temperature, the flow stresses in all cases are lower than that for room temperature specimens. Figure 3.8 shows the relative drop of peak stresses as a measure of damage of all specimens as cycling proceeds. The relative peak stress is simply the peak stress of any given cycle divided by the peak stress of the first cycle. Cumulative strain is the total strain path that the specimen experienced. From Figure 3.8, it is apparent that damage in high temperature specimens does not accumulate as fast as room temperature specimens. This effect may be due to crack healing or dynamic re-crystallization at high temperature as will be discussed in next section.

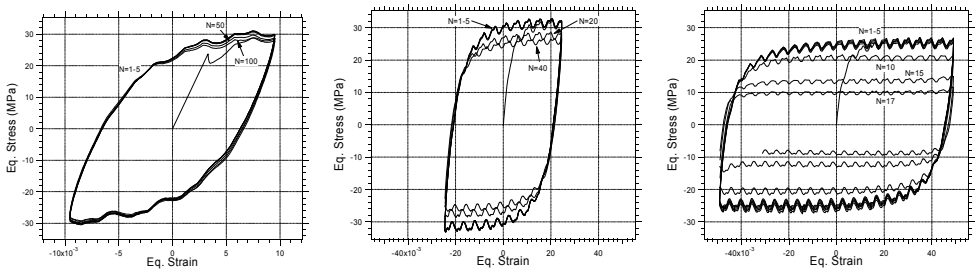

Figure 3.6. Equivalent stress-strain curves for room temperature specimens with different strain amplitude: (a) ±0.01, (b) ±0.025 and (c) ±0.05.

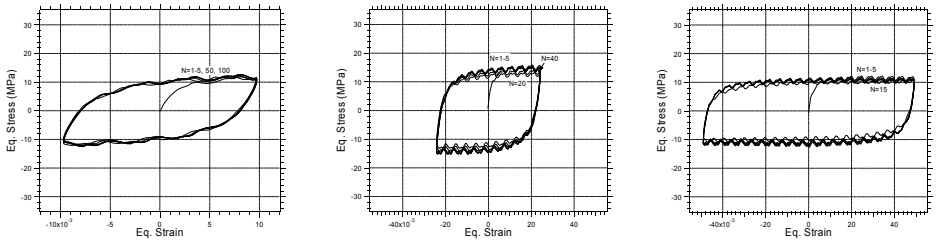

Figure 3.7. Equivalent stress-strain curves for high temperature (100°C) specimens with different strain amplitude: (a) ±0.01, (b) ±0.025 and (c) ±0.05.

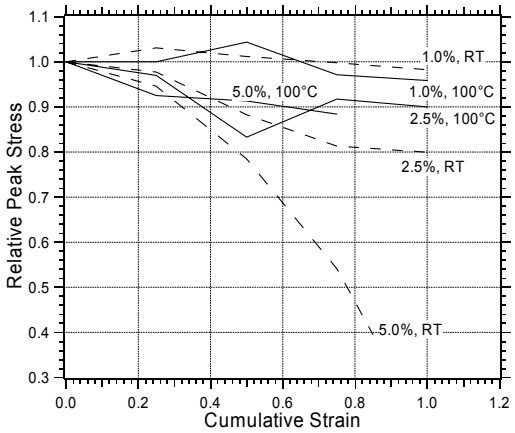

Figure 3.8. Relative stress level of various specimens as strain accumulates.

Moreover, this observation has not been noted in the literature, and the effects of high temperature on the fatigue life are rather conflicting [7,12].

The phase coarsening data are plotted in Figures 3.9(a) and (b). In this study, the Pb-rich phase size was measured using *Image Pro Plus* [11]. Figure 3.9(a) is the plot of the average Pb-rich phase sizes. The relative Pb-rich phase sizes are shown in Figure 3.9(b), where the relative Pb-rich phase-growth (RPG) is defined as:

$$RPG = \frac{\lambda - \lambda_0}{\lambda_0} \tag{3.1}$$

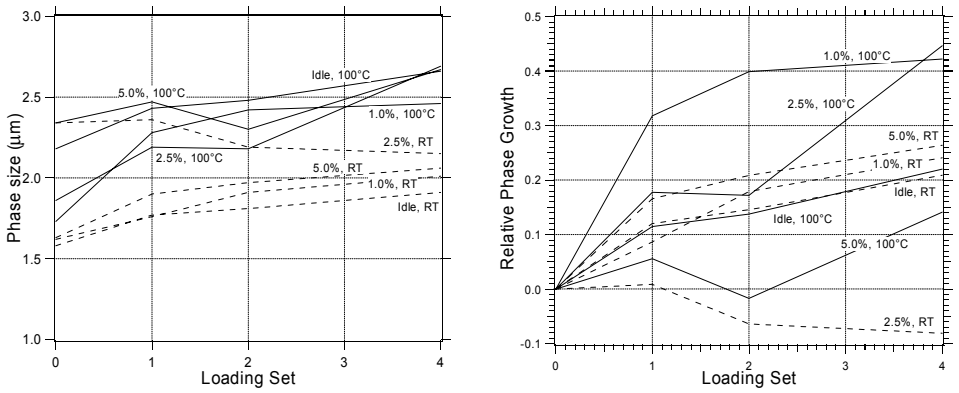

Figure 3.9. (a) average phase size, and (b) average relative phase growth according to the loading set. Loading sets were 25 cycles for 1% strains, 10 cycles for 2.5% strain, and 5 cycles for 5% strain.

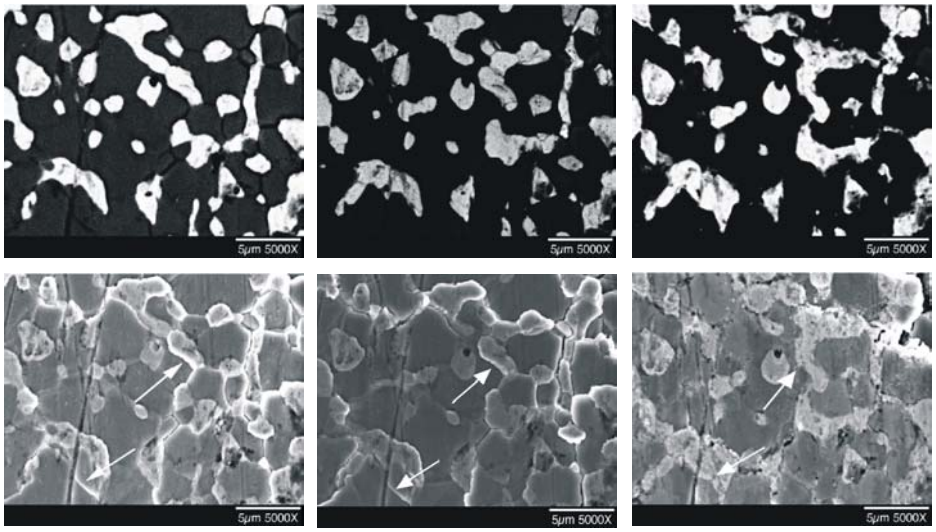

Figure 3.10. SEM Micrographs of a specific region on specimen 6107, after (left to right) 5, 10, and 20 cycles at ±5% max eq. strain at 100°C. As cycling proceeded, some microcracks became less visible and fractured Sn-rich phases fused together (as indicated by the white arrows), suggesting possible dynamic re-crystallization or crack healing at high temperature.

where λ is the current phase size and λ_0 is the initial phase size. Figures 3.9(a) and (b) show that in general, the phase coarsening is faster for the specimens that experience cycling loading combined with high temperature except the 5% case. However, the exact correlation of phase coarsening rate to temperature and load cycling is inconclusive for the current limited data.

Analysis of Figure 3.9 indicates that the mechanical contribution to coarsening is overwhelmed by the thermal contribution to coarsening under the current conditions. For a higher strain cycling case (5%), the specimen failed before any significant phase growth. It can be concluded that at room temperature, the coupling effects of aging and strain cycling is minimal.

At high temperature, however, the microstructural evolution is interesting. Figure 3.10 shows the changes of microstructure during the ±5.0%, high temperature fatigue. The top row images are back-scattered electron micrographs, showing distinct phases, and the bottom row images are secondary SEM images showing the physical features clearly. The first column is after loading set 1, the second column is after loading set 2 and the third column is after loading set 4. During early cycling, microcracks were developed along phase boundaries or within Sn-rich phase; however, later in the cycling, the cracks between different phases became less visible, suggesting that at high temperature, re-crystallization or crack healing may have occurred and retarded the damage rate. The data for high temperature strain-enhanced coarsening is still very limited, and more experiments are needed.

At room temperature, the phenomenon of crack healing or re-crystallization was not observed. Figure 3.11 shows SEM images at a specific location on the room temperature, ±5.0% strain specimen. The layout of these SEM images is the same as Figure 3.10. It clearly shows the damage was initiated early in the load cycling. The microcracks typically formed between two different phases. As cycling proceeded, no new microcracks were formed, only the existing microcracks grew deeper and wider. These distributed microcracks are thought to be a barrier for Pb-rich phase coarsening.

High temperature torsional fatigue was repeated at a slower rate to study the effect of strain rate on grain growth rate. The 5.0% equivalent strain cycling at 100°C was repeated at a lower strain rate of $10^{-5}s^{-1}$. The cyclic stress-strain response is shown in Figure 3.12. It was apparent that the flow stress was lower than that of a higher strain rate as shown in Figure 3.7(c). Also, the decreasing rate in peak flow stress is much lower than that at room temperature, Figure 3.6(c), and is more similar to that shown in Figure 3.7(c). The phase sizes as plotted against number of cycles and loading time are shown in Figure 3.13(a) and (b), respectively. The data for high strain rate experiments are also plotted in the same figures for comparison. It appears that the grain growth rate of coupled cycling/high temperature correlates more with the number of cycles than the loading time, Figure 3.13(a). Since the data is limited, the low strain rate test is inconclusive at this stage.

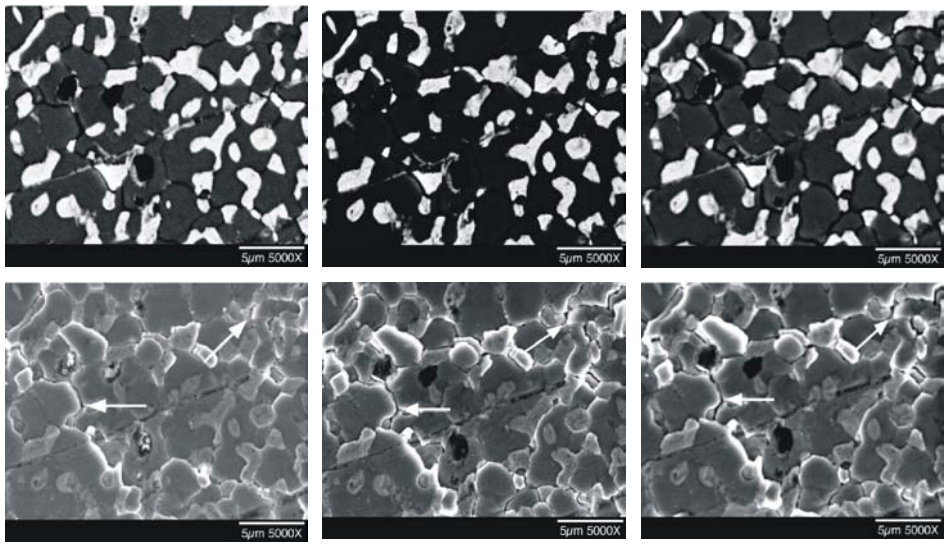

Figure 3.11. SEM Micrographs of a specific spot on specimen 6103, after (left to right) 5, 10, and 20 cycles at ±5% max eq. strain at room temperature. As cycling proceeded, no new microcracks were formed, but the existing cracks became wider and deeper (as indicated by the white arrows).

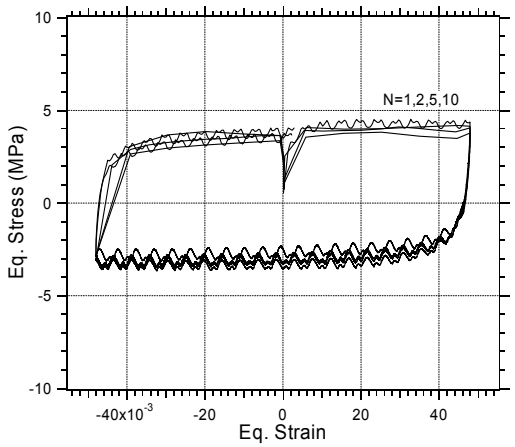

Figure 3.12. Equivalent stress-strain response as cycling proceeds for low strain rate cycling.

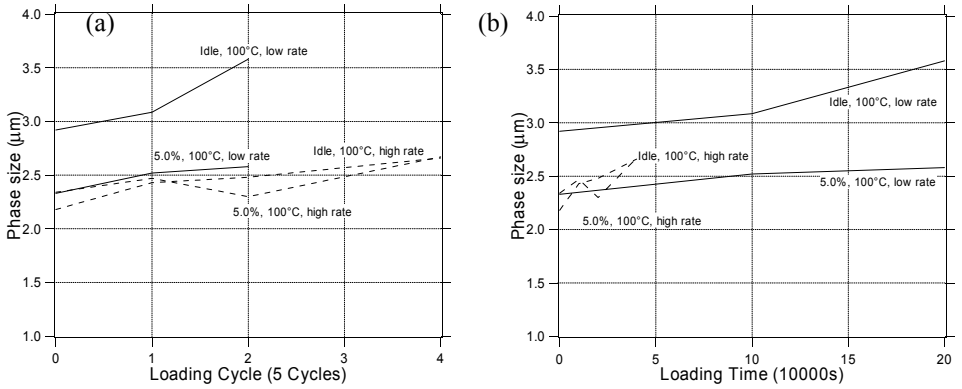

Figure 3.13. Phase size for low strain rate cycling against (a) loading cycle numbers, (b) loading time.

The phase growth data can be compared with existing models [3,9]. The model given by Vianco et al. [3] was chosen because it predicts strain-enhanced coarsening at constant temperature. The phase growth formula by Vianco et al. is given as:

$$\lambda = \lambda_0 + \{[4.10\times10^{-5} e^{-11023/T} + 15.6\times10^{-8} e^{-3123/T} (d\gamma / dt)]t\}^{0.256} \quad (3.2)$$

where λ and λ_0 are the current phase size and initial phase size in mm, respectively; T is the temperature in K; $d\gamma/dt$ is the strain rate in s^{-1}, and t is total time in s. Figure 3.14 shows the theoretical phase growth of the current test matrix using Equation (3.2). However, in comparing the experimental measurements in Figure 3.9, we see that although the data of idle specimens at room temperature is close between experiments and theory, the theoretical phase growth data with loading appear to be exceedingly high. The

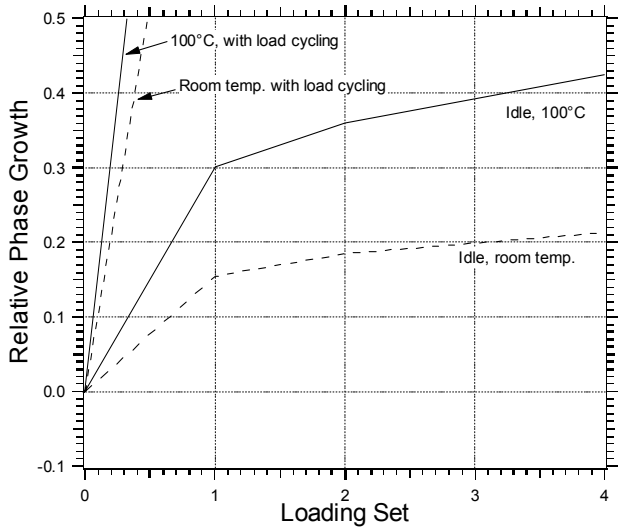

Figure 3.14. Relative Pb-rich phase growth of isothermal fatigue experiments predicted by model [3].

discrepancy may be that Equation (3.2) is based upon a thermal mechanical fatigue (TMF) data of Hacke et al. [9]; while the data from this work are isothermal data. Furthermore, only two to three specific regions on the surface of the specimens in this study were traced, which may be not enough produce statistically representative phase growth data.

3.4. Thermal Cycling

It has been reported that phase coarsening rate is faster during thermo-mechanical cycling [9] than as would be predicted from the simple superposition of thermal- and strain-induced coarsening. In the last section, the discrepancy between the coarsening data measured from isothermal cycling and the model predicted phase growth rate was presented, where the model parameters were based on thermo-mechanical cycling data. Thermal cycling tests were performed to study the phase growth phenomenon. As shown in Figure 3.15, a Sun Systems EC1A programmable thermal chamber was used to provide the thermal cycling environment.

Figure 3.15. Thermal Chamber used in Thermal Cycling tests.

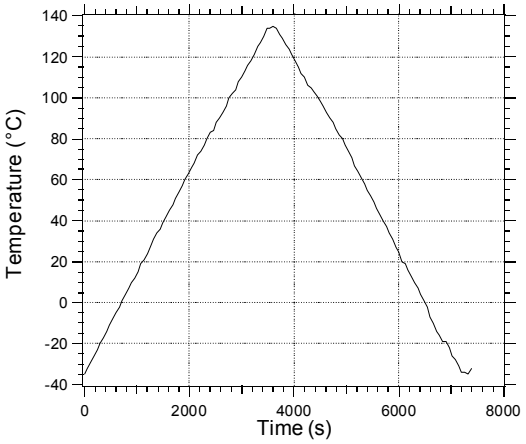

Figure 3.16. Typical temperature profile recorded during experiment.

A Keyence model VH-8000 microscope was placed at the side of the thermal chamber, so that the displacement of test specimens inside the chamber could be monitored through the thermal chamber window. The monitor on the right side of the figure displays the gage section of the specimen. Digital images can be saved for analysis.

A thermal cyclic loading

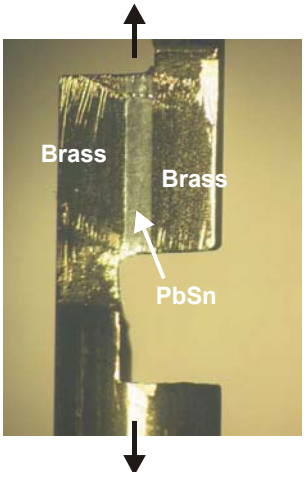

Figure 3.17 Shear Specimen used in thermal cycling tests.

profile between -35°C and 135°C with a temperature rate of 3°C/min, about two hours per cycle, was programmed for all thermal cycling experiments. Figure 3.16 displays the temperature versus time plot of a typical thermal cycle as recorded during the experiment.

In the thermo-mechanical fatigue tests, all specimens were of shear lap type as shown in Figure 3.17. The dimensions of the PbSn gage section were: length = 2.0 mm, width = 0.5mm, and thickness = 0.5 mm. The shear lap specimen was used because phase growth rate is observed to be higher in shear than in uniaxial tension.

Three type of tests were conducted: (1) Idle: the specimen was placed inside the thermal chamber without any loading. (2) Thermo-mechanical fatigue (TMF): the specimen was clamped in a loading frame, the loading frame was made of brass outer fixture and steel loading fixture, the mismatch in thermal expansion between brass and steel will cause a displacement cycling in the specimen as temperature cycles. The experimental setup and schematics are illustrated in Figure 3.18. The dimension of the load frame was set such that the equivalent shear strain experienced in the specimen was 1.0% at the peak amplitude of the thermal cycle. (3) Creep: the specimen was clamped in a loading frame, and a dead weight was hung on one end of the specimen, such that the specimen was creeping under the weight during thermal cycling. The average shear stress in the solder was about 2.0 MPa. The setup is shown in Figure 3.19.

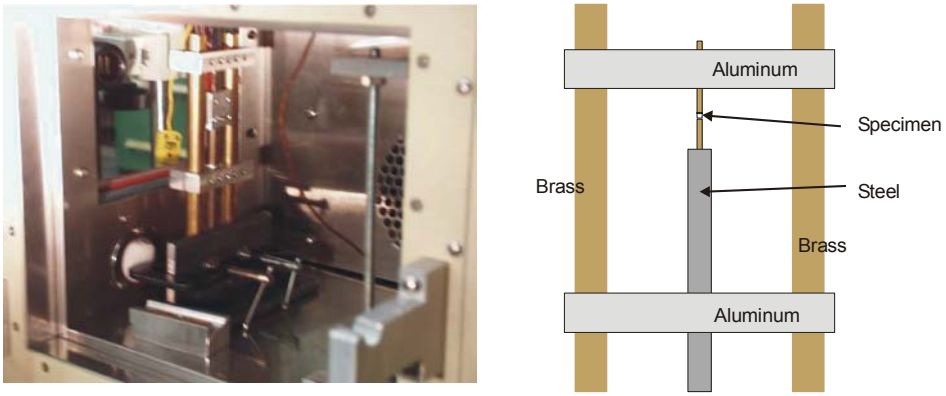

Figure 3.18. Fixture for TMF: (a) inside the thermal chamber, (b) schematics

Similar to the procedures used in the isothermal fatigue, thermal cycling was interrupted several times during the experiment to measure the Pb-rich phase size at predetermined locations. The resulting phase growth data were plotted in Figure 3.20(a) and 3.20(b) as the absolute average phase size and the relative phase growth, respectively. The relative phase growth was actually found to be less for either TMF or creep than for the idle specimens!

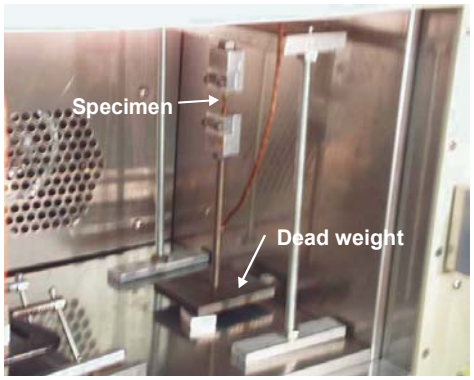

Figure 3.19. Creep fixture.

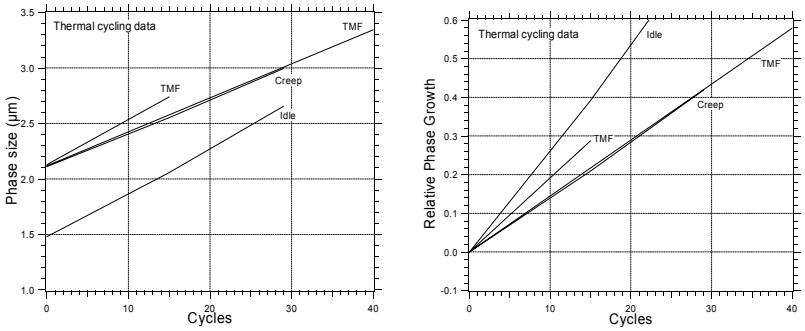

Figure 3.20. Phase size plotted against thermal cycles of all different loading modes, (a) absolute phase size and (b) relative phase growth

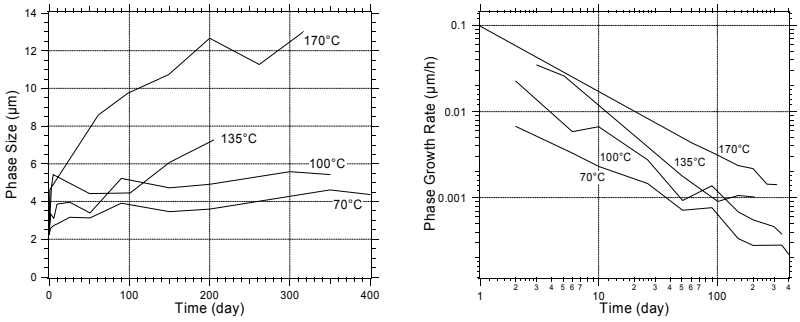

Figure 3.21. (a) Phase size data as provided by Vianco et. al. [3], (b) Growth rate calculated from the same data.

The data of the current experiment was then compared to the isothermal aging data published by Vianco et al. [3]. The size of the Pb-rich phase, and the phase growth rate for different temperature, were plotted against time in Figure 3.21(a) and (b).

Notice that in Figure 3.21(b), the growth rate decreases with time. The phase growth rate for the initial 2-3 days were estimated to be 0.0067μm/h and 0.023μm/h, respectively for isothermal aging at temperature 70°C and 100°C. For the thermal cycling between -35°C and 135°C, the phase growth rate is about 0.018μm/h, which is in-between the isothermal phase growth rate of 70°C and 100°C. This shows the phase growth rate for thermal cycling does not differ much from the isothermal phase growth rate.

In a closer examination of the surface of the creep specimen, Figure 3.22(a) and (b), the deformation was concentrated at the brass-PbSn interface, as evidenced by the scratch mark across the specimen which was initially straight. At a higher magnification, Figure 3.23, it shows that the distance between the Pb-rich phases is further apart then that far from the interface. It is possible that at a higher creep rate (heavier dead weight) or a higher strain level, the phase growth rate may become higher.

3.5. Summary of Cyclic Loading

Using equivalent strain as a variable, the fatigue life of solder in uniaxial tension-compression is consistent with torsion cycling. Experimental results indicate that the specimen with a longer aging treatment, which has a larger Pb-rich phase size, has a longer fatigue life.

Experimental procedures were developed to track microstructual evolution during fatigue. Microstructural damage and coarsening was investigated. Comparing the results of isothermal fatigue at room temperature and at 100^{o}C, the damage accumulation at 100^{o}C appears slower than at room temperature. Some microcracks would gradually disappear at 100^{o}C. Strain enhanced coarsening is not obvious at room temperature; although it is noticeable at some high temperature cases, it is less than or about the same order of magnitude of isothermal aging.

Results from thermal and thermo-mechanical cycling show that the growth rate of Ph-rich phase under thermal cycle does not differ much from the coarsening rate under isothermal fatigue, which is not in agreement with some results reported in the literature [9]. Since the experiment conditions were different, the strain rate effect may short-circuit the diffusion or coarsening process in the current experiments. Another possible reason for the discrepancy is that the current studies use the surface microstructure to imply overall microstructural response. The local stress and diffusion rate may be different between surface and bulk.

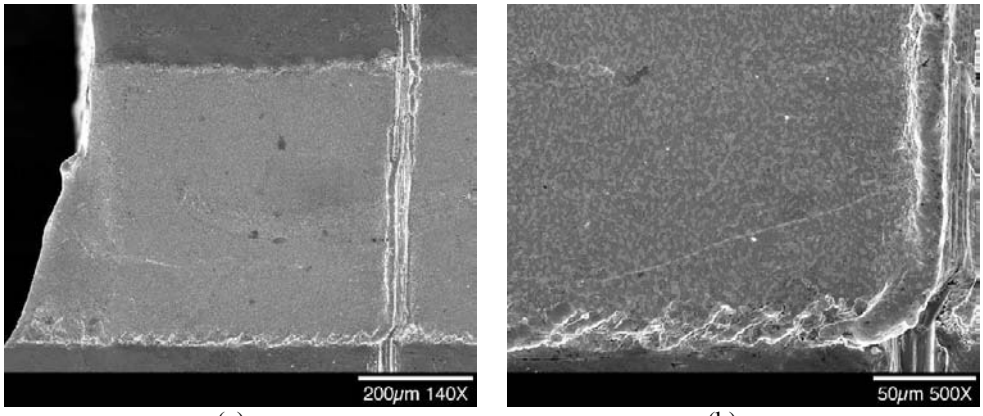

(a) (b)

Figure 3.22. SEM images of thermal cycling creep specimens near the brass interface (a) 140X and (b) 500X.

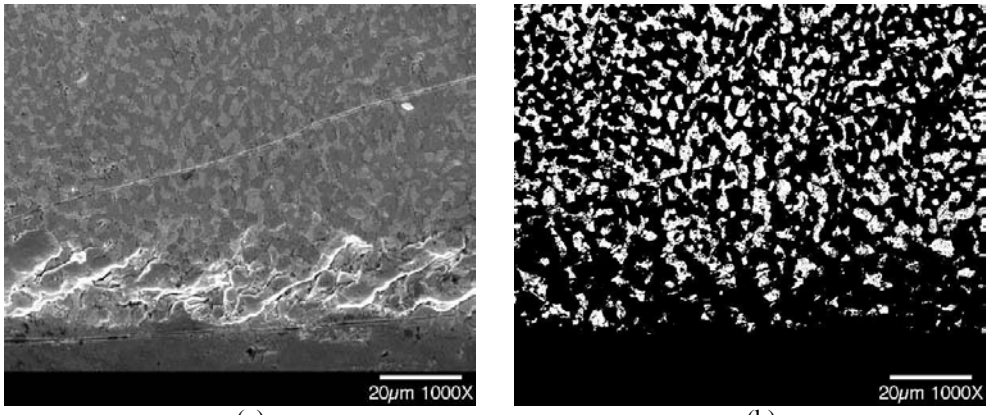

(a) (b)

Figure 3.23. SEM images of thermal cycling creep specimens near the brass interface at 1000X, (a) Secondary image, (b) back-scattered image.

4. Multiaxial Creep

4.1. Background on Creep of 63-37 Solder

4.1.1. Constitutive Relationships

The kinetics of creep behavior in metals at high homologous temperatures is often described by the Dorn constitutive relationship:

$$\dot{\gamma}_p = A\frac{Gb}{kT}D\left(\frac{\tau}{G}\right)^n\left(\frac{b}{d}\right)^p \tag{4.1}$$

where the plastic shear strain rate, $\dot{\gamma}_p$, is predicted from the shear modulus G, Burger's vector b, temperature T, diffusion constant D (itself temperature dependent), applied shear stress τ, and grain or phase size, d. For any particular creep mechanism, the values of the constant A, the stress exponent n, and the grain size exponent, p are unique, as well as the activation energy Q which enters into the Arrhenius relationship for the diffusion coefficient.

Material creep behavior is often represented with deformation mechanism maps, which delineate the various mechanisms of creep. An example deformation mechanism map for the Sn-Pb eutectic alloy is shown in Fig. 4.1. The isotherms shown in Fig. 4.1 have a constant slope within the various mechanism regions, and the slope ($\partial \ln \dot{\varepsilon} / \partial \ln \tau$) is the stress exponent n.

In the case of eutectic Pb-Sn, there are as many as six distinct regions of deformation summarized with their corresponding stress exponents, and grain size exponents in Tables 4.1 and 4.2, respectively. The differences in grain size exponent can be rationalized based on the operative mechanisms for each region. Regions I, II, and H.T.S. are associated with superplasticity and have a grain size exponent of 1.6 to 2.3, consistent with the notion that grain boundary sliding is the mechanism which allows the superplasticity. Region III is associated with power-law creep, where the creep process is associated with the climb of dislocations around intragranular obstacles, and therefore is insensitive to the grain size. Coble

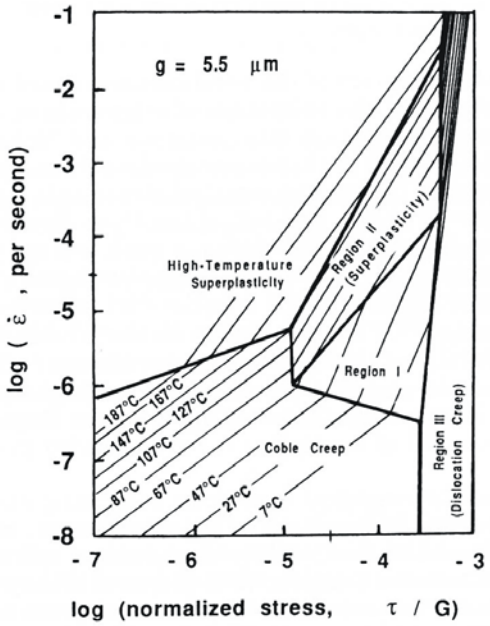

Figure 4.1. Deformation mechanism map proposed for eutectic Sn-Pb solder with an equiaxed grain size of 5.5 μm. Extracted from [9] based on the work of Pink, Marquez and Grinberg [13].

creep is associated with mass transport along grain boundaries, and is therefore strongly sensitive to the grain size, with an exponent of 3. The relative stress dependency of the various regions is also somewhat intuitive: the regions associated with diffusion are weakly stress dependent (exponent of 1), the regions associated with grain boundary sliding are moderately stress dependent (exponents of 1.6-3), and the regions associated with dislocation motion are strongly stress dependent (exponents of 3-10).

Table 4.1. Values for the stress exponent, n, in eutectic Pb-Sn

Region	***Ref. [9]***	***Ref. [13]***	***Ref. [15]***
Coble Creep		1	
Region I	1.7-3	2.84	3.0
Region II	1.6-2.4	2.08	1.65
Region III	3-7	9.1	
Region IV	>7		
High Temp. Superplasticity		1.72	

Table 4.2. Values for the grain size exponent, p, in eutectic Pb-Sn

Region	***Ref. [9]***	***Ref. [13]***	***Ref. [15]***
Coble Creep		3	
Region I	2.3	2.3	2.3
Region II	1.6-2.3	2	2.3
Region III	0	0	
Region IV	0		
High Temp. Superplasticity		2	

4.1.2 Strain-Enhanced Microstructural Coarsening

Materials undergoing superplastic flow have been shown to exhibit grain growth or microstructural coarsening at rates faster than observed in the absence of superplastic flow. This microstructural coarsening has been observed in the Sn-Pb eutectic alloy in cases where the initial microstructure is fine, unbanded, and equiaxed; otherwise the alloy may exhibit microstructural refinement early in the deformation, followed by eventual coarsening [1].

The extensive study by Clark and Alden [14] on a single phase Sn-1Bi alloy provides the basis for current-day understanding of the mechanism and kinetics associated with strain-enhanced coarsening, although the extension of this work to the behavior of eutectic Sn-Pb is not firmly established. Clark and Alden found that the additional grain growth Δg (above

and beyond purely thermal grain growth, g_A) produced during superplastic deformation scaled approximately linearly with the amount of strain ε:

$$\frac{\Delta g}{g_A} = m\varepsilon \qquad (4.2)$$

where the slope m is constant for a particular strain rate, as illustrated in Figure 4.2. The notion that in the superplastic regime the amount of excess grain growth is proportional to strain has also been observed in other alloys including a Zn-22Al-0.5Cu eutectoid with a microstructure similar to eutectic Sn-Pb [16].

Clark and Alden attributed this behavior to the formation of excess vacancies during grain boundary sliding, which was thought to accelerate the diffusion kinetics of coarsening.

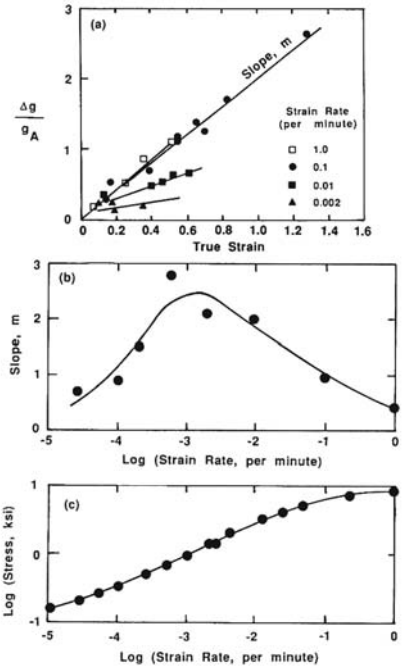

Figure 4.2. Excess grain coarsening, Δg, due to superplastic strain in a Sn-1Bi alloy shows an approximately linear relationship with the level of strain. This coarsening rate is most sensitive to strain at moderate strain rates in the vicinity of 10^{-3} min^{-1}. Extracted from [9] based on the work of Clark and Alden [15].

4.1.3 Steady-State Creep Rate and Rupture-Time under Multiaxial Conditions

The driving force for secondary or steady-state creep under multiaxial loading conditions has almost invariably been described by the Von Mises equivalent stress (e.g. [17-19]). Under assumptions of material isotropy and incompressibility, the relevance of the Von Mises criterion can be derived directly from deformation theory, and has been verified numerous times experimentally [20]. Nevertheless, there are some examples where the creep strain behavior appears to be better described by an alternative predictor, such as the maximum principle stress used to describe creep strain behavior of an Alloy 800H pressure vessel under combined axial loading and internal pressure [21]. For this reason, it is useful to verify the validity of the Von Mises equivalent stress, especially in the case of solder where the components are commonly loaded under multiaxial conditions yet experimental data is largely collected in either pure tension or pure shear (rarely both in the same study).

The driving force for creep-rupture under multiaxial loading conditions is less clear than for secondary creep. Constitutive relationships between the applied stress and rupture time are typically of the form:

$$t_f = M\sigma^{-\chi} \tag{4.3}$$

where t_f is the time to failure, M and χ are empirical constants, and σ is a stress parameter used to describe the driving force. In uniaxial behavior, the stress term could simply be taken as the applied tensile stress. Under multiaxial conditions, the Von Mises stress is one possible stress parameter, although its applicability near final failure is questionable. An alternative to the Von Mises stress is the maximum principle stress, although multiple authors [22,23] have suggested that the validity of the maximum principle stress is dependent on the degree of triaxiality. For this reason, empirically-determined combinations of the Von Mises stress and maximum principle stress has also been used to predict creep rate [22,24]. Specific to the eutectic solder alloy Sn-Pb-0.5Re, Li, Hongyuan, and Yiyu [25] have suggested that the Von Mises stress actually works better than the maximum principle stress, at least under the notched conditions of their study.

Alternatively, Nix, *et al* [26], have proposed a parameter termed the principle facet stress, based on an estimate by Anderson and Rice [27] of the average tensile stress acting on grain boundary facets perpendicular to the maximum principle stress. This average stress is related to the three principle stresses, $\sigma_1>\sigma_2>\sigma_3$, by the following approximate relationship:

$$\sigma_{PFS} = 2.24\sigma_1 - 0.62(\sigma_2 + \sigma_3) \tag{4.4}$$

In some cases, the principle facet stress has been found to be a more useful parameter for describing rupture times under multiaxial conditions than the Von Mises stress (e.g. [21]) or maximum principle stress (e.g. [28]), yet Nix, *et al*, points out that the parameter is not valid in cases where the material is sufficiently brittle such that failure is better described by crack propagation rather than uniform cavitations.

4.2. Method for Multiaxial Creep Testing of Solder

The specimen geometry chosen for multiaxial creep testing of solder was a thin-walled tubular specimen. As shown in Figure 4.3, the solder portion of the tube was 0.64 mm long constrained between two copper or brass tubes. The thickness of the tube in both the solder and copper/brass regions was 0.64 mm and the overall diameter of the tube was 6.35 mm (thickness to diameter ratio of 10:1, to establish thin-walled behavior). Therefore, the solder portion of the tube was in the shape of a ring with a 6.36 mm outer diameter

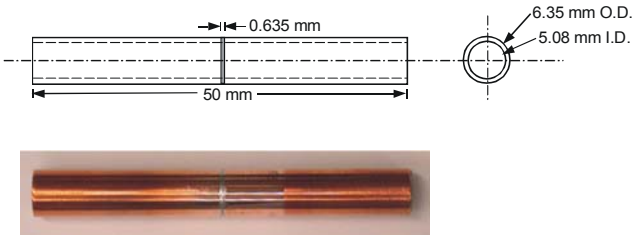

Figure 4.3. Thin-walled tube specimen containing a square-cross-section solder joint used for multiaxial creep testing of solder. The wall-thickness of the tube was 0.635 mm and the thickness-to-diameter ratio was 1:10. The left and right halves of the tube were fabricated from brass or copper.

and a square cross-section of 0.64x0.64 mm^2. The 0.64 mm cross-section was chosen to be similar to the size scale of surface mount technology solder joints in service. The tubular geometry allowed both pure tension and pure torsion of the tube as well as any intermediate mixture of tension and torsion. As will be discussed in section 4.2.3, the elastic constraint of the brass/copper tubes on the solder joint prohibited pure tension from being transmitted into the strongly constrained solder joint. Nevertheless, off-axis stresses caused by this elastic mismatch were <20% of the axial stress under tensile loading.

4.2.1 Processing Method

The processing route used to produce these tubular solder specimens strongly influences the resulting microstructure and therefore the observed properties. This non-trivial task proved to be one of the largest drawbacks to the tubular geometry. A number of processes were evaluated to determine the processing route that produces solder joints with minimal porosity, adherent solder-brass/copper interfaces, homogeneous/consistent microstructure, and minimal processing-induced damage. The fabrication process that was found to produce the most reproducible and desirable solder joints is outlined below.

1. The starting stock was a monolithic copper tube with an outer diameter of 6.35 mm and an inner diameter smaller than the eventual target 5.08 mm (Fig. 4.4a).
2. A 0.64 mm deep x 0.64 mm wide circumferential channel was lathe-machined into the central portion of the tube (Fig. 4.4b)
3. After a flux of alpha 611 and isoproplyl in a ratio of 1:1 was applied to the channel, the tube was dipped in a molten bath of solder contained in an ultrasonic solder pot. (Fig. 4.4c) The ultrasonic excitation of the molten solder proved to prevent the formation of porosity in the solder joint.
4. The excess solder, which overfilled the channel, was carefully removed through a mild lathe-machining step. The interior diameter of the tube was bored out to the desired 5.08 mm diameter, thereby removing the underlying brass/copper structure, which connected the two ends of the tube. This resulted in a solder joint that was connected to the copper/brass tube only on both ends.
5. After final machining, each specimen was annealed at 100°C for 16 hr to normalize the starting microstructure.

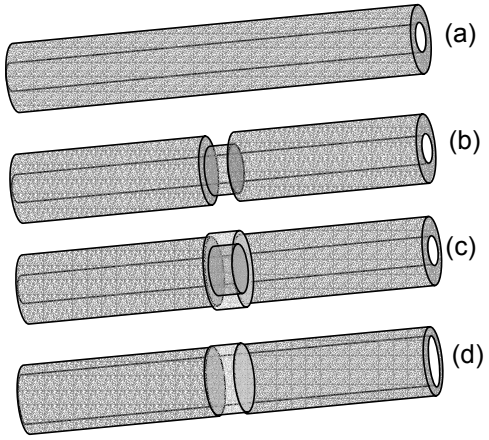

Figure 4.4. Illustration of processing steps used to produce the tubular solder joint specimen. The darker gray material is copper or brass and the lighter gray material is solder.

Alternative processing routes that did not produce desirable results were:

1. Bringing the ends of two independent tubes 0.64 mm – 1 mm away from each other; placing a solid solder precast in the gap and melting the precast.
2. After step 2 above, placing the channel-cut tube into an aluminum mold and pouring molten solder into the mold, thereby filling the channel cavity. While the resulting specimen geometry was acceptable, the solder joints were often found to contain significant porosity.

The primary disadvantage to the accepted processing route was the lack of careful control on the cooling rate. Although the specimens were all cooled in the same manner, the lack of cooling rate control produced an undesirable distribution in the size of the as-fabricated microstructure.

4.2.2. Multiaxial Creep Tester

The multiaxial creep test frame, custom built for this program, is shown in Figure 4.5. Two dead-weight hangers were used to apply constant axial and torsional loads independently. Creep displacements were observed in the axial direction using a LVDT displacement sensor and in the torsional direction using a high-precision rotary encoder. The resolution of the axial and torsional sensors were found to be better than 1 μm and 0.001° respectively. The two signals, as well as a thermocouple signal were continuously recorded using a Labview-based data acquisition system. Three multiaxial creep frames were used to enable a reasonable throughput, as these experiments can last several days to weeks. The data acquisition system acquired data from all three creep frames independently, allowing each test frame to be stopped or started regardless of the state of the other frames.

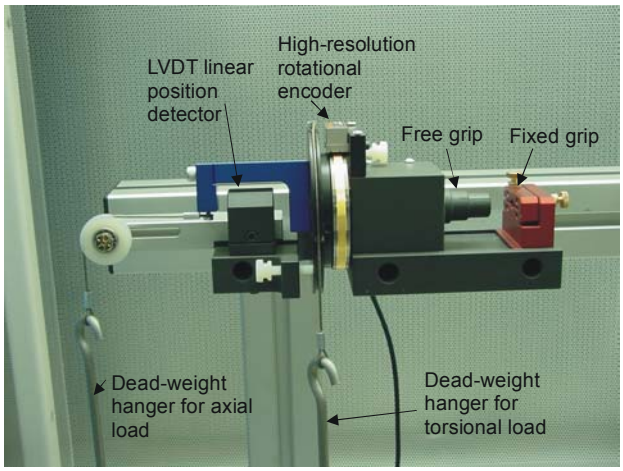

Figure 4.5. Multiaxial creep test frame. Tubular specimen fits between the fixed grip and the free grip. The free grip is unrestrained in the axial and rotational direction. Data from the LVDT linear motion detector and rotational displacement encoder are recorded periodically on a time basis.

Unintended thermal fluctuations due to building heating and air conditioning were found to produce undesirable apparent strain associated with differential thermal expansion. For example, a 2.5°C increase in temperature was observed to

produce a ~4 μm displacement in the LVDT. This temperature swing was observed as a daily cycle. The apparent strain rate due to such a thermal fluctuation was 10^{-7} s^{-1}. To minimize this problem the room was independently temperature controlled at all times by the building HVAC system. Temperature was continuously monitored at the specimen surface and recorded in conjunction with the elongation and rotation data. The largest temperature fluctuation over a one-week period was kept to less than 1°C,

4.2.3. Stress-state of solder joint

The elastic mismatch between the solder joint and the adjoining brass/copper tubes prevented the stress state at the solder joint from exactly matching the nominal stress condition estimated from force-over-area type calculations. Under tensile load, for example, the solder, which has a Poisson's ratio ~0.43 was constrained by the adjoining brass tubes with a Poisson's ratio ~0.34. This constraint imposed a multiaxial stress state and a stress gradient within the joint even under uniaxial applied forces.

This difference between the nominal applied stress and the actual stress gradient induced by elastic mismatch was quantified using elastic finite element modeling (FEM) via ABAQUS code [29]. The elastic model utilized modulus values of 15 GPa and 110 GPa and Poisson ratios of 0.43 and 0.34 for the solder and brass materials respectively. Tension and/or torsion forces were applied in the brass at nodes far from the solder or the solder/brass intersection. The FEM mesh is shown in Fig. 4.6. The results shown in the figure represent three cases: pure tension, tension plus torsion, and pure tension; in each of the three cases, the applied force(s) were chosen such that the nominal far-field Von Mises stress, as estimated from simple elastic approximations (e.g. force-over-area) was 15 MPa for all three cases. However, the local stresses in the solder joint were quite different from the nominal far-field stresses. The statistics of the distribution in Von Mises stress within the solder joint, is summarized in Table 4.3, as well as a histogram representation shown in Fig. 4.7. Although the far-field applied Von Mises stress was the same for all three loading conditions, the average Von Mises stress in the joint was substantially different for each condition: 23% below 15 MPa in the case of pure tension and 13% above 15 MPa in the case of pure torsion. While each of the three conditions had some gradient in stresses through the solder joint, the tensile condition was most pronounced, with a standard deviation of more than 2 MPa.

In subsequent work, these elastic mismatch differences were partially mitigated by choosing far-field applied forces such that the average Von Mises stresses in the solder joint were identical for the various loading conditions (i.e. tension or torsion). Fig. 4.8 shows the stress state for three loading conditions, where the far-field forces were chosen to establish an average Von Mises stress of ~15.5 MPa for each condition. Nevertheless, it was not possible to match the entire stress field, but only the average stress.

.

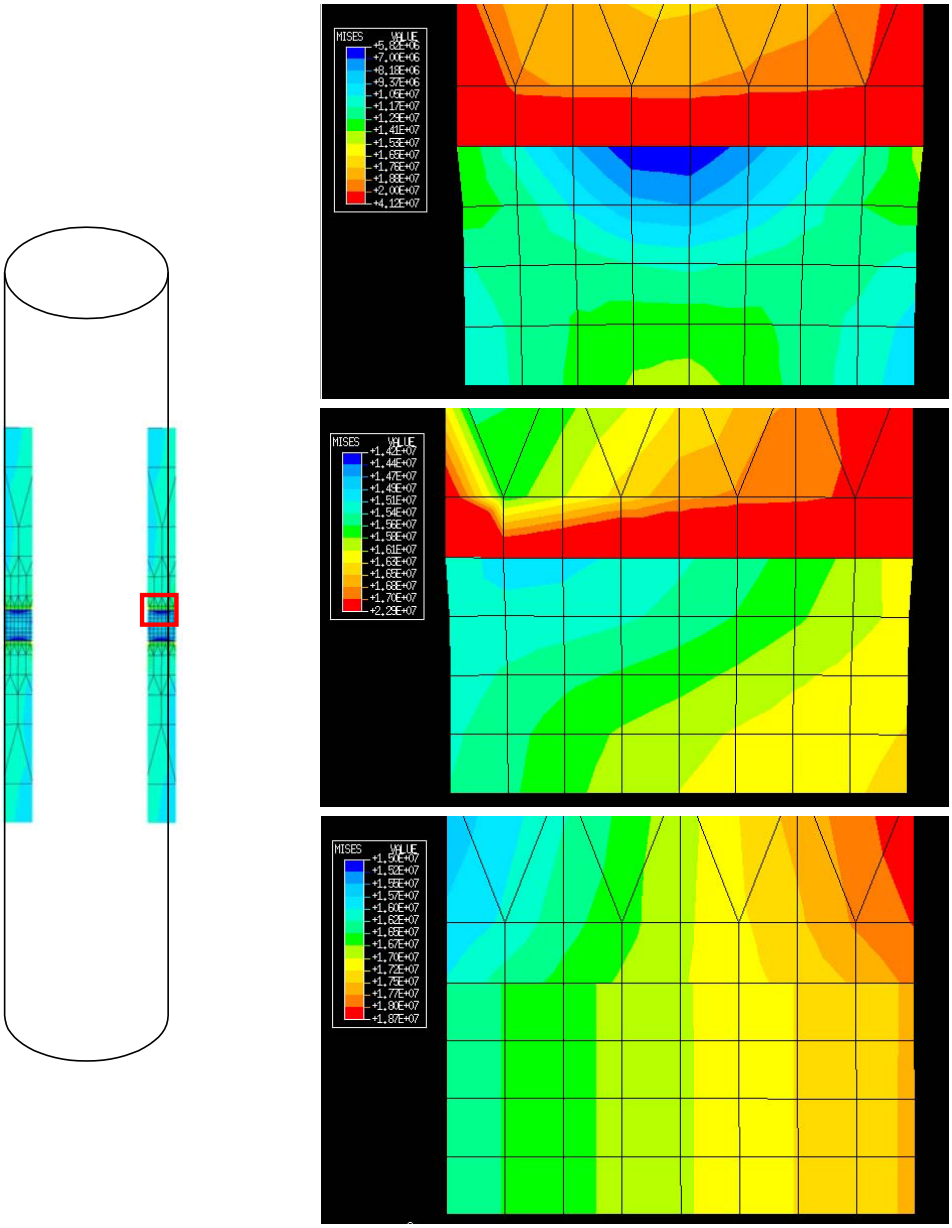

Figure 4.6. (left) Schematic of the finite element mesh with respect to the specimen geometry. Red outline is region of interest for results shown on the (right). The three results on the right represent the actual stress distribution in the case where the nominal Von Mises stress was 15 MPa as calculated from elasticity approximations for tension (top), tension plus torsion (middle), and torsion (bottom). Scale ranges are in MPa.

Table 4.3. Statistics of Von Mises stress distribution taken over all integration points within the 32 elements contained in the solder.

	Tension	***Tension+Torsion***	***Torsion***
Average Von Mises Stress (MPa)	11.51	15.74	16.95
Standard Deviation (MPa)	2.09	0.37	0.35

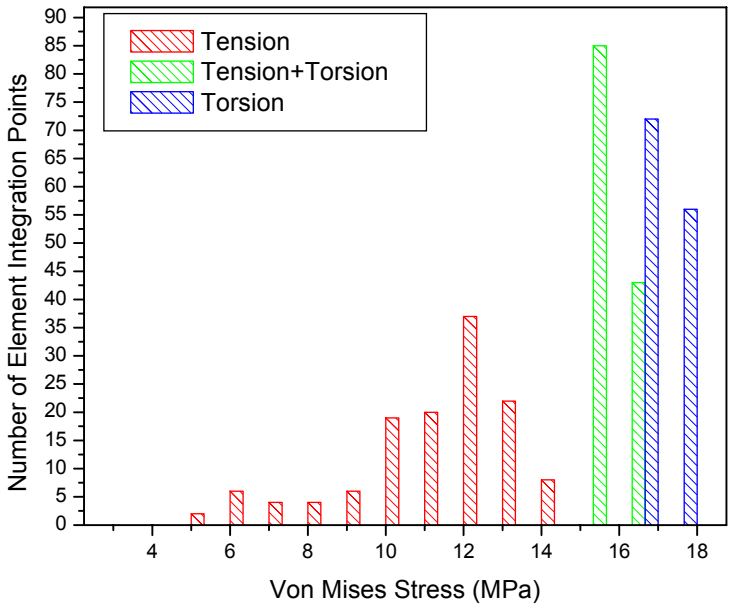

Figure 4.7. Distribution of Von Mises stresses through the solder joint under three far-field loading conditions. In each of the three cases, the far-field (nominal) Von Mises stress was 15 MPa. Far-field tension produced the widest distribution of stresses within the solder joint.

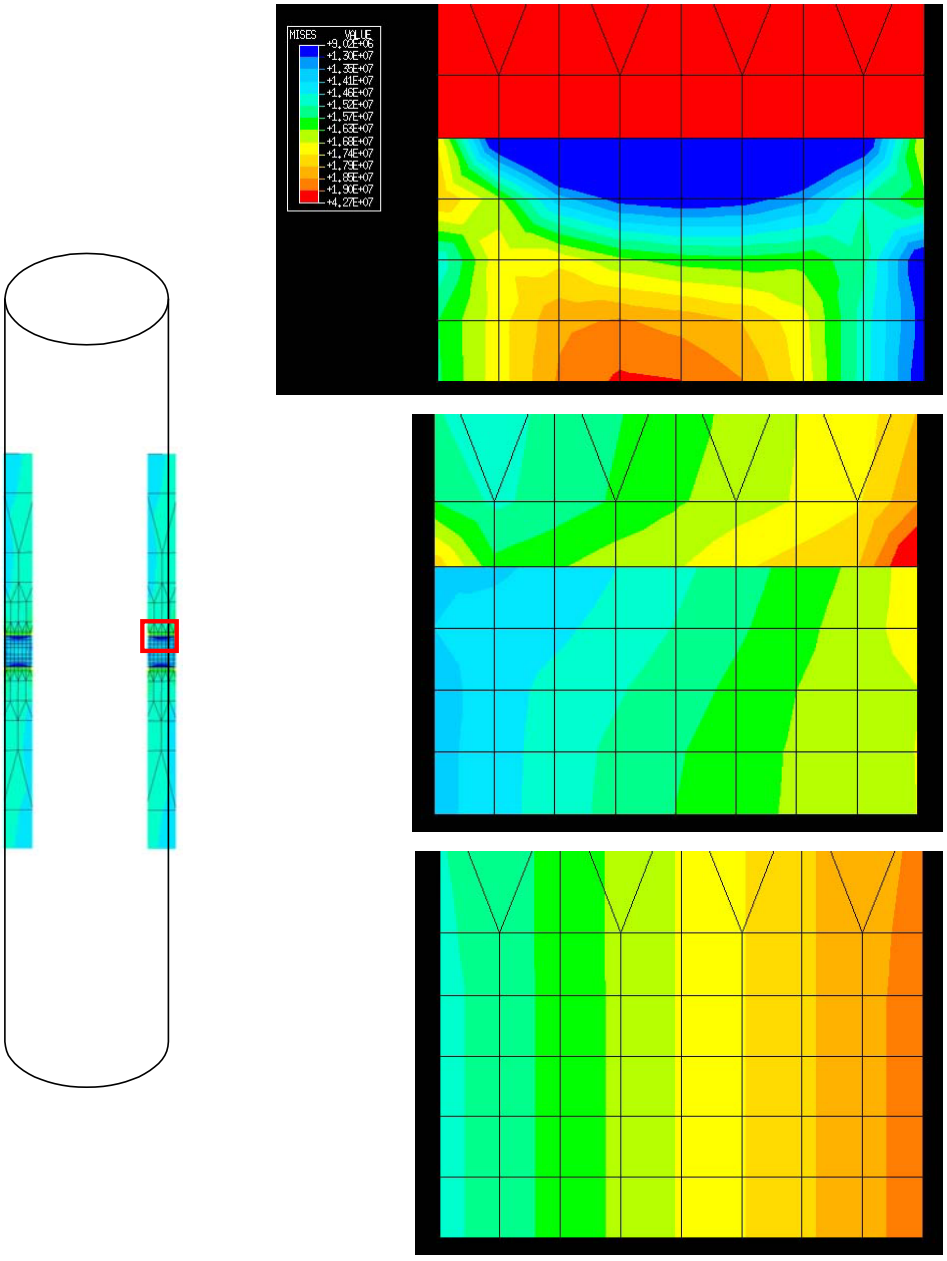

Figure 4.8. Stress distribution in solder joint when the applied forces are chosen such that the average Von Mises stress in the solder portion of the joint (bottom four element rows) is 15.5 MPa in tension (top), tension plus torsion (middle) and torsion (bottom). The stress scale (in MPa) is the same for all three results.

4.2.4. Evolution of stress-state during creep

The creep straining process itself can cause a redistribution of stresses. To estimate the redistribution of stresses within the solder specimen, the creep process was evaluated using the simple ABAQUS creep power law model [29]:

$$\dot{\bar{\varepsilon}} = A\sigma_{VM}^{n} t^{m} \tag{4.5}$$

where the time-dependant average creep strain rate, $\dot{\bar{\varepsilon}}$, is related the Von Mises effective stress, σ_{VM}, the creep time, t, and the temperature-dependent pre-exponent term A. To emulate the experimentally observed tensile creep behavior of solder at room temperature, with applied tensile stresses in the vicinity of 15 MPa, the value of A was set as $1.2\text{x}10^{-26}$, n was set to 3.16 for σ_{VM} in units of MPa, and m was set to –0.65 for t in units of s. Elastic properties were set identical to the values defined in the previous section. The stress distribution of the solder joint constrained between the brass tubes was observed in the purely elastic state as well as after periodic creep times up to ~17 hr, where tertiary creep would cause imminent rupture. The results, summarized in Fig. 4.9, indicate that there was only minimal redistribution of stresses associated with the creep process. Specifically, the largest change in Von Mises stress was an increase of ~10% observed at the solder-brass interface at the outside edge of the tube. Most of the solder joint was predicted to experience <5% change in applied Von Mises stress during the creep process.

4.3. Results – Constitutive Behavior

Creep behavior was characterized by monitoring the evolution of specimen elongation and rotation with time. Typical raw-data creep curves, with absolute elongation normalized into strain, are shown in Fig. 4.10 for the tube solder joint specimens under uniaxial tension, showing the well-established three-stage sigmoidal shape. The minimum creep rate associated with secondary creep was taken at the shallowest portion of the strain-time curves. This minimum creep rate, along with time to failure and loading conditions, was characterized for every creep experiment and is tabulated in Appendix 1. For the case of combined tension and torsion, the Von Mises stress is described in cylindrical coordinates by:

$$\bar{\sigma}_{VM} = \frac{1}{\sqrt{2}}\left[2\sigma_{zz}^{2} + 6\sigma_{\theta z}^{2}\right]^{1/2} \tag{4.6}$$

where σ_{zz} is the tensile component of applied stress and $\sigma_{\theta z}$ is the shear component of applied stress. Equivalently, the effective strain is described by:

$$\bar{\varepsilon}_{eq} = \frac{\sqrt{2}}{3}\left[(\varepsilon_1 - \varepsilon_2)^2 + \varepsilon_2^2 + \varepsilon_1^2\right]^{1/2} \tag{4.7}$$

where ε_1 and ε_2 are the principle components of strain, related to the tensile strain ε_{zz} and the shear strain $\gamma_{\theta z}$, by:

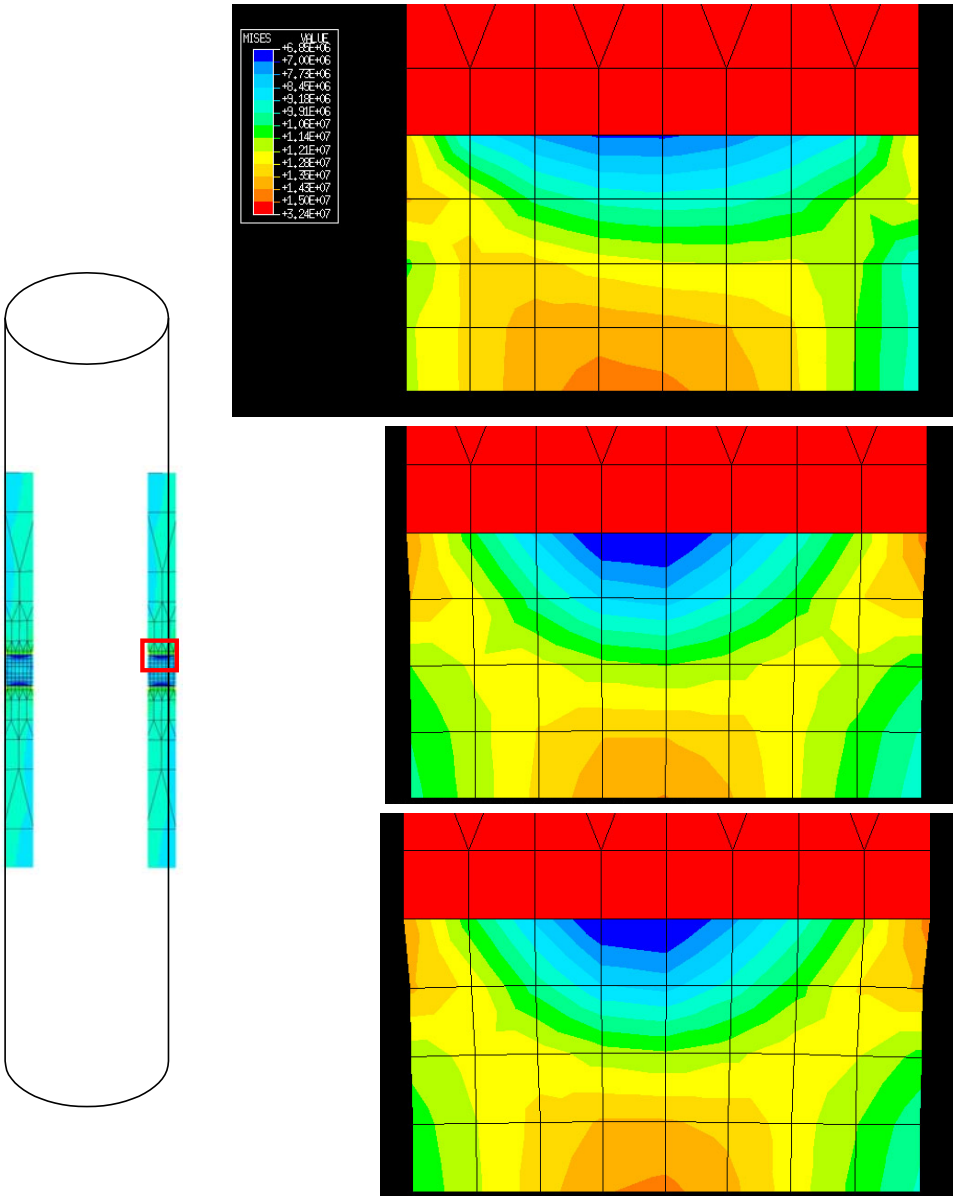

Figure 4.9. Stress redistribution during creep under a tensile stress of 15.5 MPa after 0 hr (top), 3.3 hr (middle) and 16.7 hr (bottom). The stress scale (in MPa) is the same for all three results.

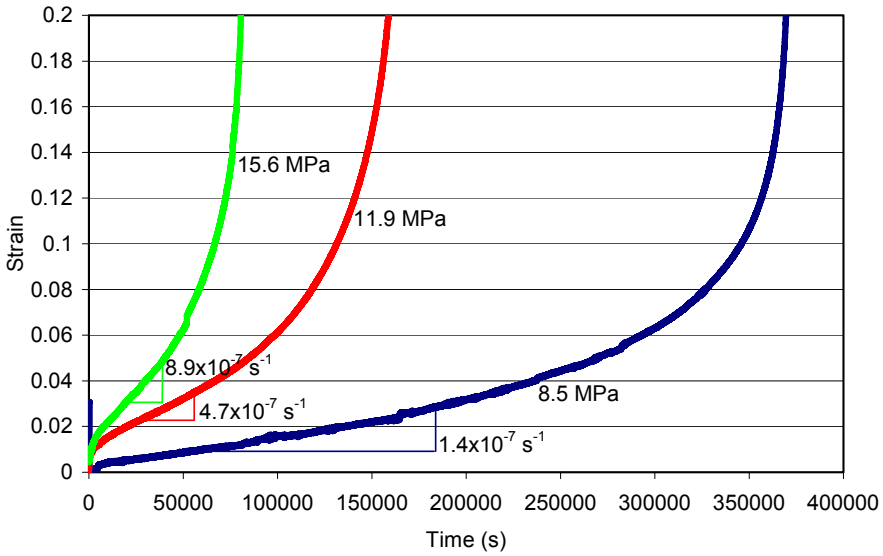

Figure 4.10. Typical strain-time creep curves observed under uniaxial tension with the tubular solder joint specimen. The average Von Mises stress for each of the three loading conditions is labeled in units of MPa. Minimum creep rate values are labeled in units of s^{-1}.

$$\varepsilon_1 = \frac{\varepsilon_{zz}}{2} + \sqrt{\left(\frac{\varepsilon_{zz}}{2}\right)^2 + \left(\frac{\gamma_{\theta z}}{2}\right)^2} \tag{4.8}$$

$$\varepsilon_2 = \frac{\varepsilon_{zz}}{2} - \sqrt{\left(\frac{\varepsilon_{zz}}{2}\right)^2 + \left(\frac{\gamma_{\theta z}}{2}\right)^2} \tag{4.9}$$

4.3.1. Steady-state Creep Behavior

The minimum creep rate is plotted as a function of average applied Von Mises stress in Fig. 11, comparing two data sets collected at room temperature under uniaxial tension. The data set collected from an earlier processing method, which suffered from significant void formation throughout the solder joint, showed significantly more scatter than the data set collected using the "current" void-free processing method. Nevertheless, a significant degree of scatter was found to persist with the improved processing method. This scatter was thought to be attributable to the lack of careful control on the cooling rate and ensuing

microstructural phase size. To validate this notion, the as-fabricated Pb-rich phase size was measured for three specimens prior to creep. As expected, the creep rate scaled inversely with the coarseness of the microstructure. The degree of scatter inherent in the lack of control of the starting microstructure implied the need for multiple experiments under any loading condition to establish the mean behavior.

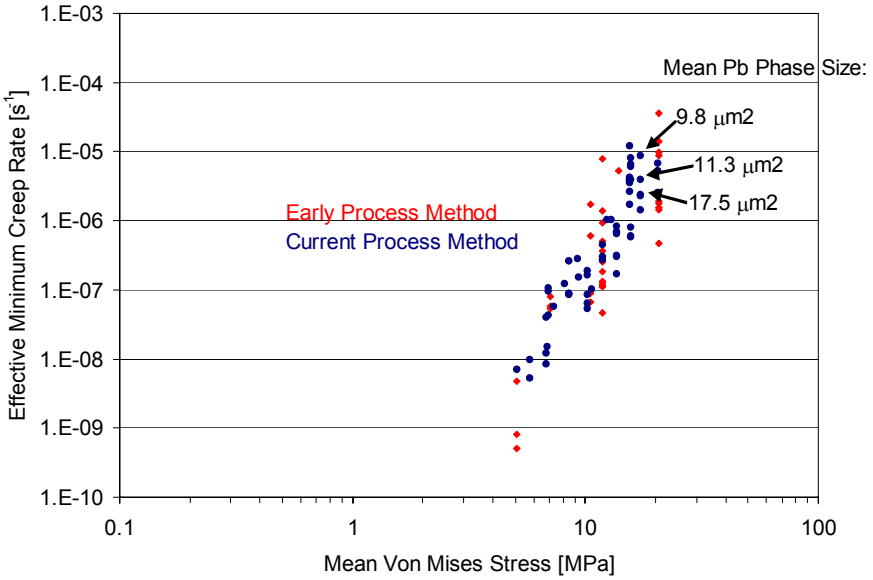

Figure 4.11. Room temperature, uniaxial minimum creep-rate data showing scatter prior to fabrication improvements (red) and after fabrication improvements (blue). The remnant scatter is largely attributed to scatter in the as-fabricated phase size.

Uniaxial tension creep data for two temperatures, room temperature and 100°C, is plotted in Fig. 4.12. Over the range of stresses and temperatures evaluated in the current study, the data appears to be consistent with the Region I creep mechanism as described in [15]. The current dataset was fit using the Garafalo hyperbolic sine relationship:

$$\dot{\varepsilon}_{\min} = A\left(\frac{d}{d_0}\right)^p \left(\sinh\left(B\sigma_{VM}\right)\right)^m \exp\left(\frac{-Q}{RT}\right) \tag{4.10}$$

where the minimum creep rate, $\dot{\varepsilon}_{\min}$, is predicted from the applied Von Mises stress, σ_{VM}, phase size, d, temperature, T, and activation energy Q, using the stress exponent, m, grain size exponent, p, gas constant, R, and constants d_0, A, and B. In the current study, the term $A(d/d_0)^p$ is combined into one constant, A', since the phase size was not explicitly varied.

Based on a least-squares regression, a best fit to the dataset was found with the following values: A' = 1x10^{8} s^{-1}, B = 0.093, m = 3.4, and Q = 85000 J/mol. The activation energy of 85000 J/mol is similar to the reported value of 84000 J/mol reported by Mohamed and Langdon [15] and the stress exponent of 3.4 is identical to the value reported by Mei, Morris, Shine, and Summers [30], although somewhat higher than the value of 3.0 reported by Stephens and Frear [31]. It is important to note that the current dataset was not configured to produce accurate values for these constants. For example, the activation energy is determined based on only two temperatures whereas a more thorough study to identify an accurate activation energy would require several temperatures. Nevertheless, the general similarity of observed constants with reported values indicates the consistency of the current dataset.

The role of multiaxial loading was studied by applying either pure tension, pure torsion (shear), or some degree of combined tension and torsion. The observed equivalent strain rate is plotted as a function of applied average Von Mises stress in Fig. 4.13. The tensile data in Fig. 4.13 is the same data as plotted in the previous figure, Fig. 4.12. It is apparent from Fig. 4.13 that the data collected under torsion or combined tension and torsion falls on top of the tensile data when plotted in this equivalent manner. While there is somewhat more scatter in the torsion data, there is no statistical evidence of a distinction between the different loading conditions. This result is not unexpected, as several researchers in the past have concluded the validity of a Von Mises equivalence approach on the multiaxial creep rate behavior of other materials. This work simply affirms the validity of this equivalence approach for eutectic solder. This affirmation is specifically important in the case of solder, where the in-service solder joints are almost invariably under multiaxial

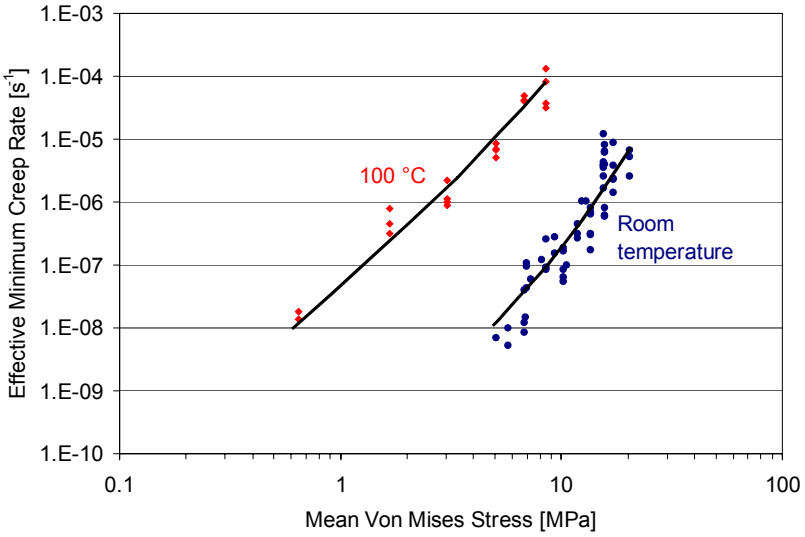

Figure 4.12. Creep behavior at room temperature and 100°C under uniaxial tension.

stress states and microstructural coarsening associated with creep is suspected to be dependent on loading condition.

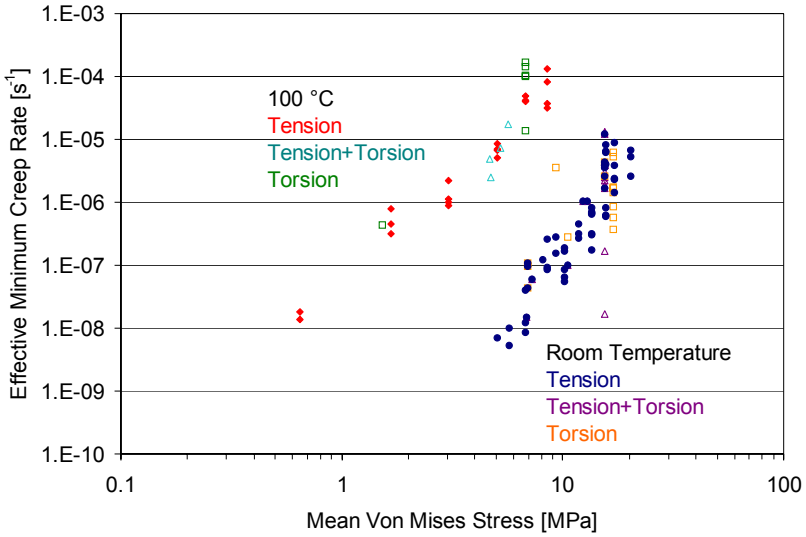

Figure 4.13. Creep behavior at room temperature and 100°C under various loading conditions.

4.3.2. Monkman-Grant product of minimum creep-rate and time to failure

The role of multiaxial loading on creep behavior can be further examined using the Monkman-Grant product of minimum creep rate and rupture time. This product is commonly shown to be constant within a given creep mechanism. The Monkman-Grant product is plotted as a function of applied average Von Mises stress for the current dataset in Fig. 4.14. Data that span four orders of magnitude in strain rate are collapsed to within a single order of magnitude using the Monkman-Grant product. Values for the Monkman-Grant product for data collected at room temperature are generally in the range of 0.02 to 0.1 whereas values for data collected at 100°C are generally in the range of 0.06 to 0.8. At room temperature there is no obvious distinction between tensile data and torsion or combined-loading data, however, at 100°C the Monkman-Grant product is seen to increase with an increasing degree of applied shear, as shown with one standard deviation of statistical significance in Fig. 4.15. This shift in the Monkman-Grant product suggests a possible change in creep mechanism, which will be explored in more detail in the following section.

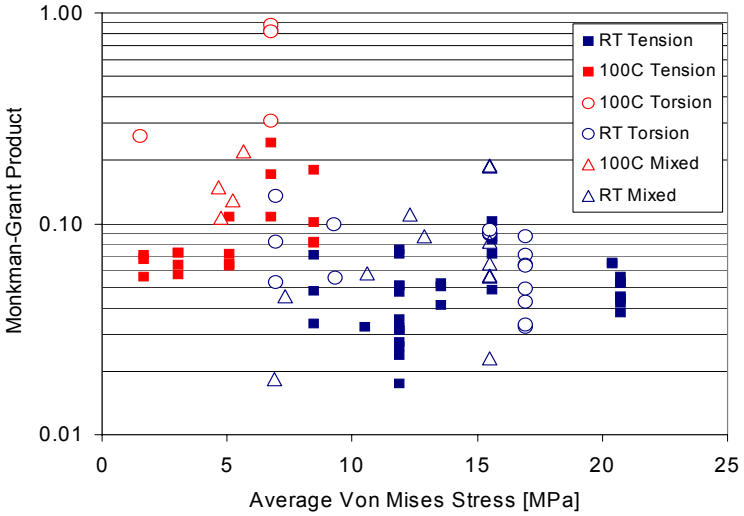

Figure 4.14. Observed Monkman-Grant product (strain-to-failure times minimum equivalent creep rate).

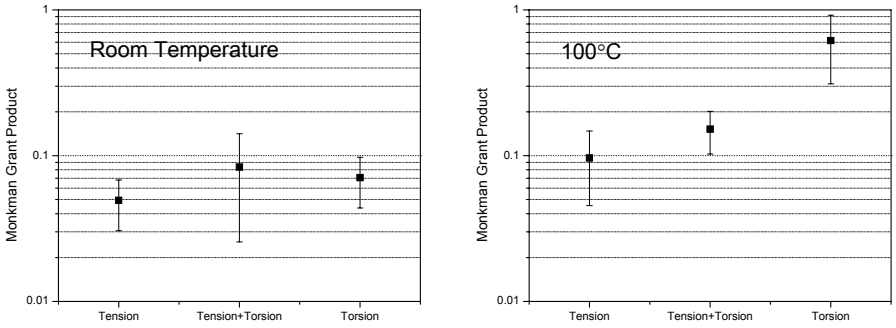

Figure 4.15. Monkman-Grant product data from Fig. 4.14 replotted to emphasize the statistical significance of the change in Monkman-Grant product at 100°C in torsion. Error bars indicate one standard deviation.

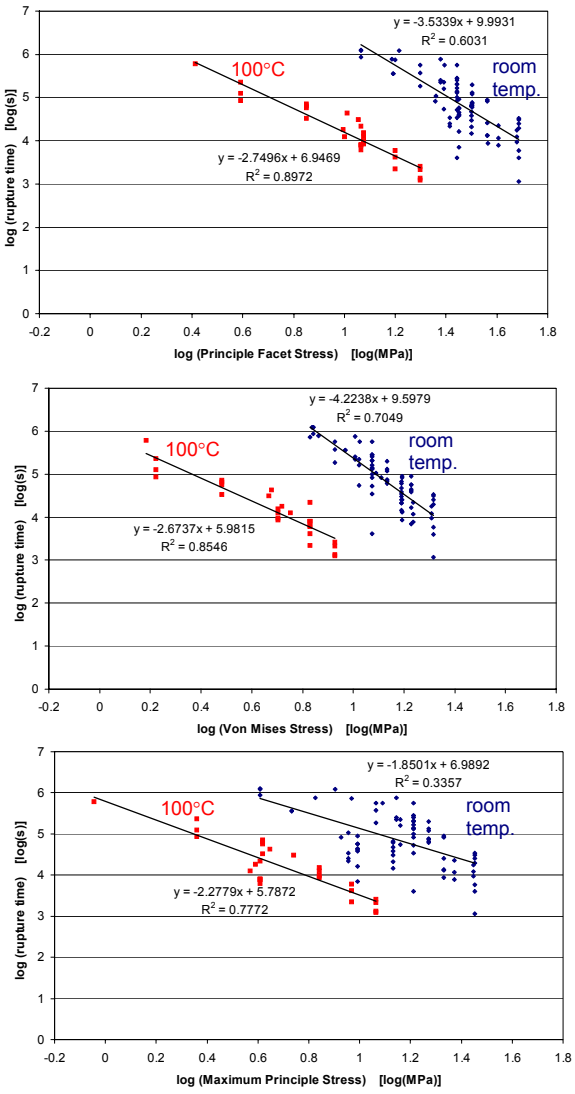

Figure 4.16. Experimental observations (data points) and predictive trends (lines) of rupture time as a function of various stress parameters: (a) principle facet stress, (b) Von Mises stress, and (c) maximum principle stress. Of these three, the best correlation coefficients were obtained with the Von Mises stress for room temperature data and the principle facet stress for 100°C data.

4.3.3. Stress parameters for predicting rupture time.

As described in the background section, there are several potential choices for a multiaxial stress parameter to establish a constitutive relationship (Eq. 4.3) between the loading condition and the creep rupture time. To determine the most predictive multiaxial stress parameter for the current dataset, the logarithm of the time to failure is plotted as a function of the logarithm of the maximum principle stress, Von Mises stress, and principle facet stress in Fig. 4.16. Of these three parameters, both the principle facet stress and the Von Mises stress were significantly better predictors than the maximum principle stress. The Von Mises stress appeared to establish a better correlation for the room temperature data, whereas the principle facet stress established a slightly better correlation for the 100°C data. Both of these parameters demonstrated capability of predicting the failure time to within half an order of magnitude, a variability that is largely attributable to observed experimental scatter. A wider range of multiaxial loading conditions (i.e. notches, pressurization, etc.) may show a stronger discrimination between these to parameters.

4.4 Results – Microstructural Evolution

4.4.1 Quantitative observations on generalized strain-enhanced coarsening.

Owing to the large distribution in starting microstructures, it is necessary to sample a large number of specimens to deduce trends in microstructural evolution in creep. This problem is further exacerbated by the inability to observe the local variability of microstructure within an individual sample. A summary of the post-test Pb-rich phase sizes for specimens after creep at an average Von Mises stress of 5 MPa and 15.5 MPa is compared to other specimens inspected after fabrication in Fig. 4.17. While the trend is consumed by statistical deviation, nevertheless a trend towards increasing Pb-rich phase size appears to exist for an increasing amount of applied tension, consistent with notions of strain-enhanced coarsening. The combined tension and torsion specimens also exhibited a slightly coarser microstructure compared to the as-fabricated condition. On the other hand, the regions sampled on the pure-torsion specimen exhibited a Pb-rich phase size very similar to that of the starting microstructure. Based on these

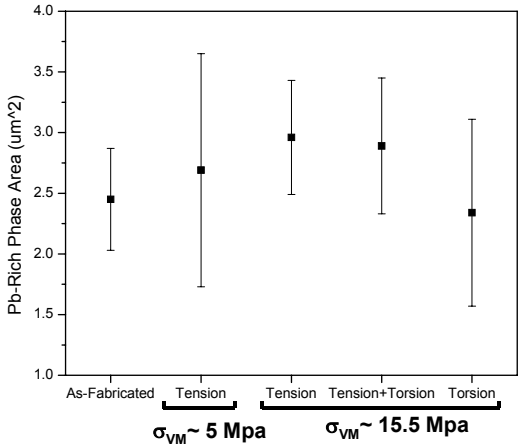

Figure 4.17. Pb-rich phase size evolution during creep. Error bars indicate one standard deviation.

observations, pure torsion appears to be less susceptible to *generalized* coarsening than pure tension or mixed tension and torsion.

4.4.2 Qualitative observations made by tracking a microstructural region during creep.

A qualitative study of the microstructural evolution induced by creep under tension and torsional loading was possible on the outer polished surface of the tubular solder-joint specimens. Micrographic montages of regions containing ~750 Pb-rich grains on the polished outer-surfaces of the tubular specimens were documented after 100ºC/16hr stabilization prior to loading. The specimens were loaded and allowed to creep through the primary creep regime, then unloaded and the same regions in the microstructure were identified and documented. This inspection occurred again near the end of the steady-state creep regime, and one final time well into tertiary creep but before final rupture. A representative subset of the montages is shown in Fig. 4.18. From this figure, the microstructural evolution is apparent both after primary creep and after secondary creep. During tertiary creep, the observed microstructure showed little further evolution, most likely because the deformation had localized elsewhere. It is interesting to note that in this set of observations, there was no clear qualitative difference in the evolution of the tension and torsion specimens.

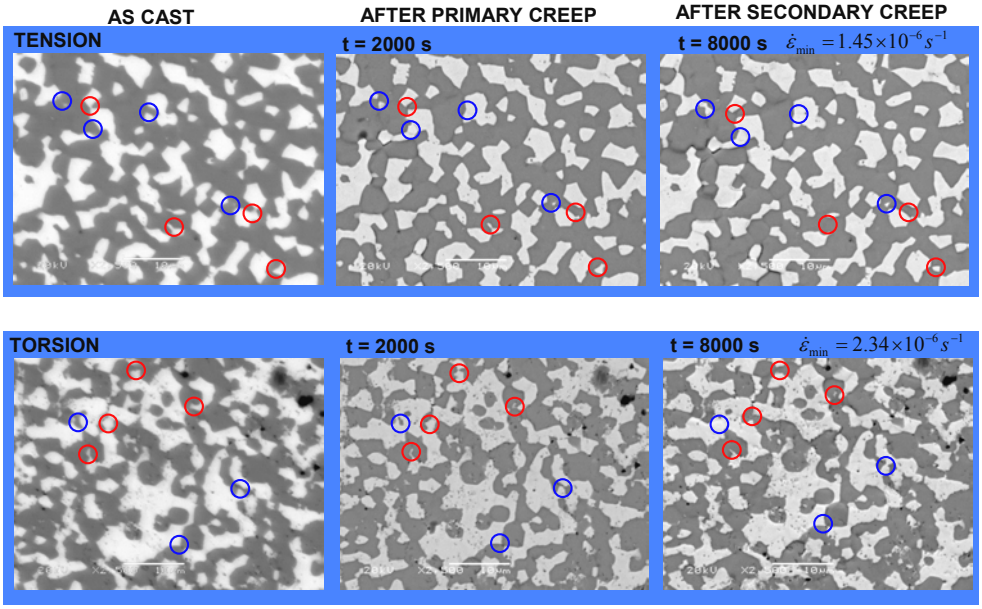

Figure 4.18. Evolution of microstructure during creep under tension and torsion loading conditions, both loaded at an equivalent Von Mises stress of 15.5 MPa at the outside surface of the tubular specimen where the inspection was made. In both cases, there were regions of Pb-rich phase growth (blue circles) and Pb-rich phase shrinkage (red circles). There were no noticeable distinctions in the generalized coarsening evolution under these two loading conditions.

4.4.3 Onset of localized coarsening under torsional loading.

Lower-magnification inspection, however, indicated that there were substantial evolutionary differences between these two conditions that were overlooked in the higher-magnification localized inspections. These differences are apparent in Fig. 4.19 where the torsion-loaded specimen showed significant coarsening localized in the vicinity of the failure. This localized coarsening was not apparent in the pure tension specimen or the combined tension and torsion specimen with 25% of the total Von Mises stress due to the tensile load. Another example of the localized coarsening under shear loading is shown in Fig. 20. The bulk of the solder joint had an average Pb-rich phase size of 2.59 μm^2 with a standard deviation of 1.00 μm^2, whereas the region of coarsened material near the solder-copper interface had an average Pb-rich phase size of 12.7 μm^2 with a standard deviation of 6.7 μm^2. In Fig. 20, the most pronounced coarsening did not appear at the interface where the dominant crack existed, but at the opposite interface. Closer inspection revealed a small region of coarsening also existing around the dominant crack.

Based on Fig. 19, the localized coarsening phenomenon appears to require nearly pure torsion and even in conditions where only 25% of the Von Mises stress is tensile, localized coarsening was not observed. To better delineate this transition from generalized to localized coarsening, creep experiments were performed at several levels of stress mixity (as described by the percentage of tensile contribution to the Von Mises stress): 100%, 50%, 28%, 14%, 7%, and 0%. These experiments were performed at two room temperature total Von Mises stress levels (16 and 10 MPa) and one 100°C Von Mises stress level (7 MPa). After failure, cross-sectional images of the microstructure near the final cleavage surface were examined for each of the loading conditions, as shown in Fig. 21. Both the high-stress room-temperature and 100°C loading conditions exhibited localized coarsening at highly torsional loading conditions and no localized coarsening under highly tensile conditions. The transition in behavior appeared to occur in the vicinity of 7-28% tension. However, for the four levels of stress mixity in the low-stress room-temperature dataset, such a trend was not apparent. In fact, under this low-stress condition, even pure tension appeared to produce localized coarsening. The strongest distinction for this low-stress room-temperature dataset from the other two datasets is that the creep rates were considerably lower ($\sim 10^{-7}$ s^{-1}) where localized coarsening was not dependent on stress-mixity than the creep rates ($>10^{-6}$ s^{-1}) where localized coarsening was dependent on stress-mixity. Therefore, based on this limited dataset, it seems plausible that localized coarsening is torsion-activated only at higher strain rates $>10^{-6}$ s^{-1} (where strain-enhanced coarsening dominates over time-dependent thermal coarsening). At lower strain rates localized coarsening appears to be activated under all observed loading conditions. This observation is based on a very limited dataset and a more thorough study of this behavior is necessary prior to seeking a phenomenological explanation.

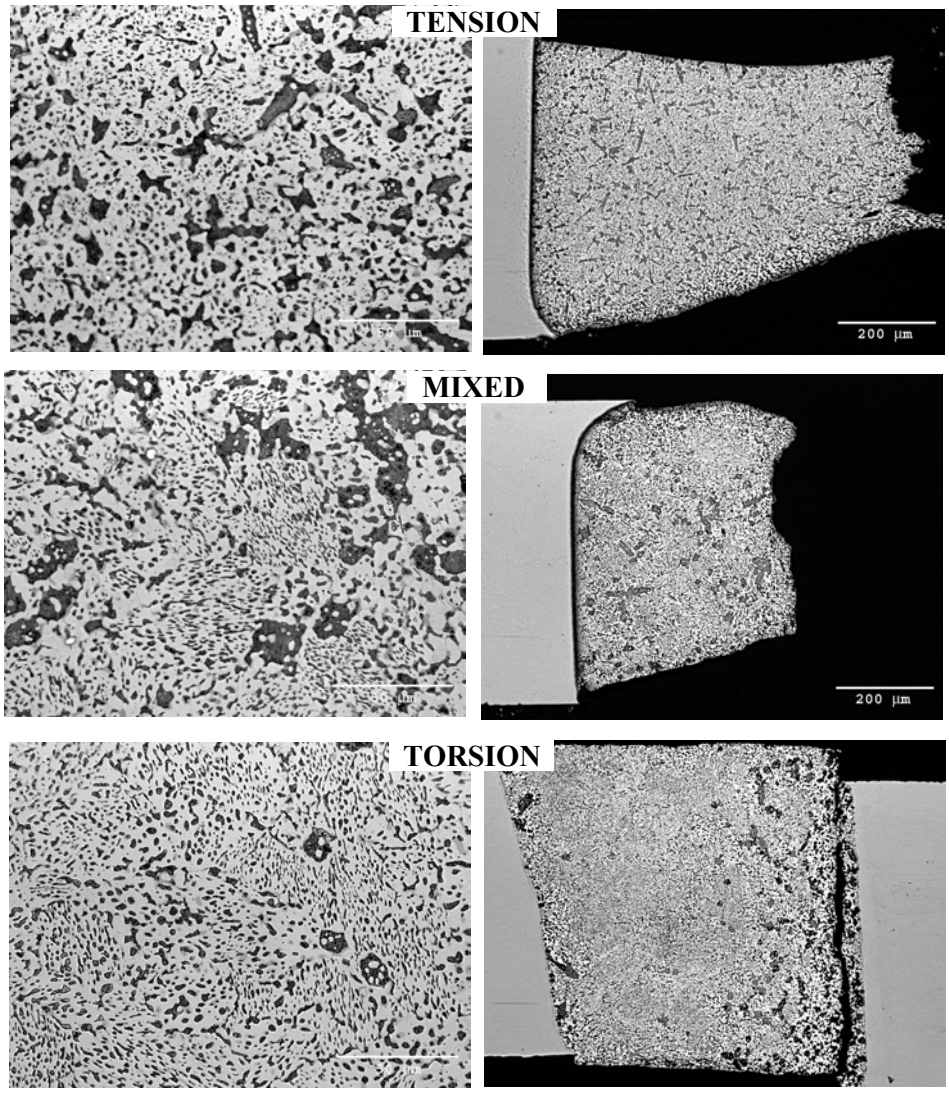

Figure 4.19. Cross-sectional microstructure after creep rupture under three loading conditions: tension, combined tension and torsion (25% tension, 75% torsion), and pure torsion. In all three cases, the average Von Mises stress during creep was 15.5 MPa.

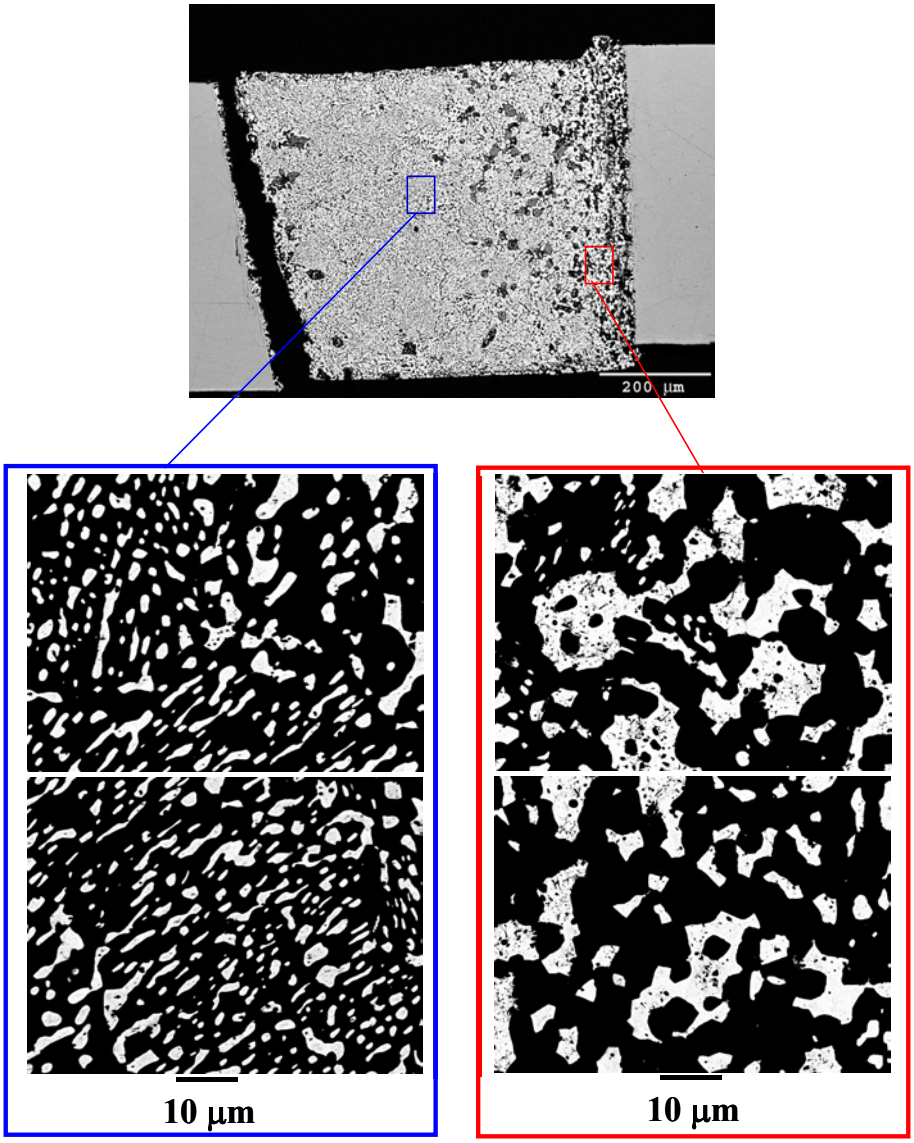

Figure 4.20. Localized coarsening (right, in red frame) associated with a high-strain region near the solder-copper interface as compared to the general microstructure (left, in blue frame).

4.5. Summary of Multiaxial Creep

1. A method for multiaxial (tension/torsion) creep testing of solder has been established using a thin-walled tube in a dead-weight biaxial test frame. The elastic mismatch between the solder joint and the brass or copper thin-walled tube creates constraint and induces a complex stress state within the solder join even under far-field uniaxial tension.

2. Creep data was collected at RT and 100°C over the creep rate range of 10^{-9} s^{-1} to 10^{-4} s^{-1}. Values obtained for the activation energy and stress exponent are consistent with published values for Region-I creep behavior.

3. Consistent with established understanding, the Von Mises equivalent stress appears to be a useful predictive parameter for describing multiaxial minimum creep-rate data.

4. At room temperature, the Monkman-Grant constant lies in the range of 0.02 to 0.10 over a wide range of stresses/strain-rates and is independent of loading condition. The 100°C M-G constant in tension (0.06 to 0.3) is slightly higher than that of RT and in torsion, the constant is considerably higher (0.3 to 0.9). This difference suggests a change in creep mechanism, and is thought to be related to the onset of localized coarsening.

5. For the current range of temperatures and multiaxial loading conditions, both the Von Mises stress and the principle facet stress showed roughly equivalent predictive capability in describing the creep rupture time. Both of these parameters were significantly better than the maximum principle stress that has occasionally been used elsewhere.

6. Post-test observations of microstructure have shown only weak correlation between creep and generalized coarsening. The relationship seems to be overwhelmed by variability in the initial phase size. Nevertheless, the trend may be interpreted to indicate that generalized coarsening is not as pronounced under torsional loading (where localized coarsening becomes active) compared to loading with a significant tensile component.

7. Tracking a local region of microstructure through the creep process indicated that there were no obvious qualitative distinctions in generalized coarsening behavior under tension or torsion loading.

8. Localized coarsening was observed under torsional loading conditions. In cases of mixed tension and torsion, where the tensile component contributed at least 25% of the total Von Mises stress, there were no indications of localized coarsening, Fig. 4.21.

9. In torsion, failure occurred in the coarsened region. In one case a coarsened zone was located in the absence of cracking, indicating that the localized coarsening leads to cracking and not the reverse. At room temperature, this localized coarsening failure did not seem to reduce the creep life (Monkman-Grant product remained constant). Instead, 100°C torsion samples actually showed substantial increase in creep life over tensile samples.

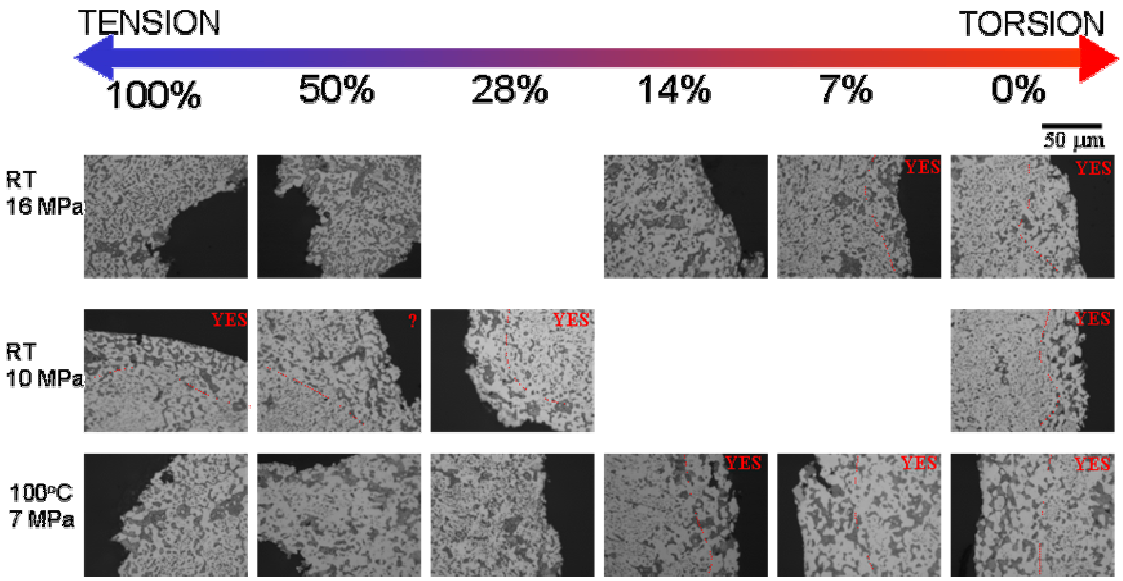

Figure 4.21. Observations of microstructure near the final fracture surface (boundary between solder and blacl by percentage of the tensile component in the total Von Mises stress for two room temperature (RT) and one 1 stress level (16 MPa, 10 MPa, and 7 MPa respectively).

5. Conclusions

Small-scale material testing capabilities have been established during this investigation. Test systems, e.g., Tytron and TorsionMaster, with very high resolutions of force/torque and displacement/rotation are available. A multiaxial creep system has been successfully designed and manufactured for the project. These systems allow a variety of loading modes for specimens with sub-millimeter dimensions, including tension, torsion, combined tension torsion, cyclic loading, creep, etc.

Various fabrication, processing, and aging treatments for solder specimens have been developed, which has enabled us to produce specimens with consistent microstructural features such as same composition, void free, and desired average phase size. Control of these parameters is very important to this study. Very small–scale solder specimens, equal or smaller than typical in-service solder joints, have been used in this experimental investigation. For example, the cross section of the smallest tensile specimen was 84x254 μm. At these small size scales, variability in phase size appears to be unavoidable. Techniques that further improve the uniformity of phase size in a specimen, e.g., methods to control cooling rate, are desired.

Finite element analysis has been used to analyze various specimen geometries and loading modes, using the bulk properties of solder, to obtain estimates for the stress distributions in the gage section. This analysis has provided useful insight into the role of constraint in the stress state of these small-scale specimens.

Tensile stress-strain behavior has been shown to be size dependent. The results show that small solder specimens do not follow bulk material properties when the cross-sectional area of the gage section is less than 0.1 mm^2. The deformation of such small specimen is not uniform and concentrates on cell boundaries, indicating cell sliding or rotation. The typical cell size was estimated to be ~40 μm. Extensively deformed small-scale tensile specimens displayed multiple necks. Such a phenomenon is not known for bulk specimens. A size effect was not observed under torsional loading, although experimental uncertainties prevented conducting torsion experiments for specimens with a diameter less than 1 mm.

The effect of microstructural size on monotonic tension or torsion is found to be minimal. This result is based on two averaged Pb-rich phase sizes, 2 and 4 μm. There is evidence that the Pb-rich phase size affected torsional fatigue life and creep rate (specimens of larger phase size had a longer fatigue life and a slower creep rate); however, the differences are small.

From results obtained for multiaxial creep experiments at room temperature and 100^{o}C, the activation energy and stress exponent are consistent with published values for Region-I creep behavior. The creep conditions explored in this study establish the aspects of a multiaxial deformation mechanism map that are typical of normal stockpile conditions. The further determination of the entire multiaxial deformation mechanism map of solder has been made possible by the current study; however this would require an onerous test matrix. The Von Mises equivalent stress appears to work well for various loading modes. For

steady-state creep-rate data, three loading conditions (tension/mixed/torsion) collapse onto a single curve using the Von Mises equivalent stress.

After intensive experimental and microstructural investigation, the coarsening phenomenon of eutectic solder is still not very clear. It is apparent that *representative* conclusions on the coarsening behavior of solder require a large number of observations to mitigate the extensive variability in both starting microstructure and response. From the data collected from isothermal torsional fatigue at 10^{-4} s^{-1}, there is no correlation between the initial phase size and the magnitude of accumulated strain experienced by the specimen. The result is the same at a strain rate at 10^{-5} s^{-1}. For the thermal cycling tests conducted, the coarsening rate is in the same order as the isothermal fatigue. These results are unexpected and contradict other data reported in the literature. Therefore, the model predicted strain enhanced coarsening appears to be exceedingly high in comparison to current data. The strain rate considered in the current experiment may be too high to trigger the strain coarsening mechanism. These indefinite conclusions on strain-enhanced coarsening may be due to confounding variability in the starting microstructure as well as differences in sampling and measurement methods. It is clear that it would be of great benefit to continue to study these issues in the future, now that a solid foundation of beginning to understand these complex and competing mechanisms has been established. For example, low strain rate experiments and low temperature experiments, which are not included in this investigation, may provide additional information to these issues.

In creep specimens, localized coarsening is observed at the failed region for some loading conditions, predominantly under pure shear, and in some combined tension and shear conditions where the tensile component of the Von Mises stress is less than 28% (low tensile contribution). Localized coarsening was also observed in high tension conditions when the steady-state creep rate was low ($<10^{-6}$ s^{-1}). When localized coarsening was observed, the coarsened region was near the solder-brass interface and often very localized to the zone near the creep crack, although in at least one case, localized coarsening was observed near the interface prior to crack formation. In addition, under equivalent Von Mises stresses, torsional loading accommodated considerably larger creep strains to failure than tension loading. The torsional condition apparently is more superplastically accommodating, in apparent conflict with the supposition that localized coarsening would promote crack formation and failure. This observation should be explored more thoroughly in the future to better understand the evolution in failure criterion under multiaxial conditions.

REFERENCES

1. Solder Mechanics – A State of the Art Assessment, Edited by Darrel R. Frear, Wendell B. Jones and Kenneth R. Kinsman, The Minerals, Metals & Materials Society, 1991.
2. Burchett, S.N., Frear, D.R., and Rashid, M.M., "Computer Simulation of Solder Joint Failure", SAND95-0086.
3. Vianco, P.T., Buchett, S.N., Neilsen, M.K., Rejent, J.A., and Frear, D.R., "Coarsening of the Sn-Pb Solder Microstructure in Constitutive Model-Based Predictions of Solder Joint Thermal Mechanical Fatigue", J of Ecletronic Materials, Vol. 28, No. 11, pp. 1290-1298, 1999.
4. Whitelaw, R. S.; Neu, R. W. and Scott, D. T., "Deformation Behavior of Two Lead-Free Solders: Indalloy 227 and Castin Alloy," *Journal of Electronic Packaging,* Vol.121, 1999.
5. Jiang, H.; Hermann, R. and Plumbridge, W. J., 1996, "High-strain fatigue of Pb-Sn Eutectic Solder Alloy," *Journal of Materials Science,* V.31.
6. Cutiongco, E. C.; Vaynman, S.; Fine, M.E. and Jeannotte, D. A., 1990, "Isothermal Fatigue of 63Sn-37Pb Solder," *Journal of Electronic Packaging,* V.112.
7. Stolkarts, V.; Keer, L. M. and Fine, M. E., 1999, "Damage Evolution Governed by Microcrack Nucleation with Application to the Fatigue of 63Sn-37Pb Solder," *Journal of the Mechanics and Physics of Solids,* V. 47.
8. Cortez, R.; Cutiongco, E. C. and Fine, M. E., 1992, "Correlation of Uniaxial Tension-Tension, Torsion, and Multiaxial Tension-Torsion Fatigue Failure in a 63Sn-37Pb Solder Alloy," IEEE Conference.
9. Hacke, P. L.; Sprecher, A. F.; Conrad, H., 1997, "Microstructure coarsening during thermo-mechanical fatigue of Pb-Sn solder joints," *Journal of Electronic Materials,* v.26, no.7, p.774-782.
10. Frear, D.R., "Thermalmechanical Fatigue in Solder Material", Solder Mechanics – A State of the Art Assessment, Edited by Darrel R. Frear, Wendell B. Jones and Kenneth R. Kinsman, The Minerals, Metals & Materials Society, Ch. 5, 1991.
11. Image Pro Plus, 2001, version 4.1.1.2, Media Cybernetics.
12. Leece, G. D., Miskioglu, I. and Nelson, D. A., 1996, "An Experimental Investigation of the Effects of Cycling Frequency and Temperature on the Fatigue Life of 60 Tin/ 40 Lead Solder," *Journal of Electronic Packaging,* V.118.
13. E. Pink, A. Marquez, and A. Grinberg, *Scripta Metall.*, 1981, vol. 15, pp. 191-194.
14. M. A. Clark and T. H. Alden, *Acta Metall.*, 1973, vol. 21, pp. 1195-1206.
15. F. A. Mohamed and T. G. Langdon, T.G., *Phil. Mag.*, 1975, vol. 32, pp.697-709.
16. D. S. Wilkinson and C. H. Caceres, *Acta Metall.*, 1986, vol. 34, pp. 97-106.
17. A. E. Johnson, *Met. Rev.*, 1960 vol. 5, pp. 447-506.
18. F. K. G. Odqvist, "Mathematical Theory of Creep and Creep Rupture," Clarendon Press, Oxford, 1966.
19. I. Finnie and W. R. Heller, "Creep of Engineering Materials" McGraw-Hill Book Co. Inc., New York, 1959.
20. N. D. Batsoulas, *Steel Research*, 1996, vol. 67, pp. 558-564.
21. S. McAllister, R. C. Hurst, and T. E. Chung, *Int. J. Pres. Vel. & Piping*, 1991, vol. 47, pp. 355-370.

22. R. J. Browne, P. E. J. Flewitt, D. Lonsdale, M. S. Shammas, and J. N. Soo, *Mater. Sci. and Tech.*, 1991, vol. 7, pp. 707-717.
23. K. Maile, *Trans. Indian Inst. Met.*, 1996, vol. 49, pp. 371-375.
24. D. R. Hayhurst and F. A. Leckie, In "Mechanical Behavior of Materials", Proc. ICM4, vol. 2, Pergamon Press, Oxford, 1984, p. 1195.
25. W. Li, F. Hongyuan, and Q. Yiyu, *Trans. Nonferrous Met. Soc. China*, 1999, vol. 9, pp. 822-825.
26. W. D. Nix, J. C. Earthman, G. Eggeler, and B. Ilschner, *Acta Met.*, 1989, vol. 37, pp. 1067-1077.
27. P. M. Anderson and J. R. Rice, *Acta Metall.*, 1985, vol. 33, pp. 409-422.
28. Y-H. Hsiao, H. Zhang, and G. S. Daehn, *Met. and Mater. Trans. A*, 1996, vol. 27, pp. 891-900.
29. Hibbit, Karlsson & Sorensen Inc. ABAQUS version 5.7 User's Manual, Hibbit, Karlsson & Sorensen Inc., Pawtucket, RI, 1998.
30. Z. Mei, J. W. Morris, Jr., M. C. Shine, and T. S. E. Summers, *J. Elec. Mater.*, 1991, vol. 20, pp. 599-608.
31. J. J. Stephens and D. R. Frear, *Met. and Mater. Trans. A*, 1999, vol. 30A, pp. 1301-1313.

APPENDIX 1. Summary of Multiaxial Creep Results

Specimen ID	Temperature (K)	Tension Load (kg)	Torsion Load (kg)	Tension Min Creep Rate (s^{-1})	Torsion Min Creep Rate (s^{-1})	Average Von Mises Stress (MPa)	Effe Strair (s
BR6337A	298	15.45	0	9.00E-07	0	10.51	6.00
BR6337C	298	15.45	0	1.36E-07	0	10.51	9.08
BR6337D	298	15.45	0	1.00E-07	0	10.51	6.67
BR6337-11	298	17.45	0	1.70E-07	0	11.87	1.14
BR6337G	298	17.45	0	1.40E-06	0	11.87	9.34
CU6337A	298	17.45	0	7.58E-07	0	11.87	5.05
CU6337B	298	17.45	0	2.79E-07	0	11.87	1.86
BR6337H	298	17.45	0	2.06E-06	0	11.87	1.37
BR6337I	298	17.45	0	5.56E-07	0	11.87	3.71
CU6337E	298	17.45	0	1.17E-05	0	11.87	7.80
BR6337M	298	17.45	0	1.66E-07	0	11.87	1.11
CU6337F	298	17.45	0	2.01E-07	0	11.87	1.34
CU6337I	298	17.45	0	7.03E-08	0	11.87	4.69
CU6337J	298	17.45	0	1.93E-07	0	11.87	1.29
CU6337K	298	17.45	0	3.85E-07	0	11.87	2.57
CU6337L	298	17.45	0	1.76E-07	0	11.87	1.17
CU6337R	298	6.45	0.58	4.59E-07	6.94E-06	15.50	4.02
CU6337S	298	6.45	0.58	3.46E-07	5.22E-06	15.50	3.02
CU6337T	298	6.45	0.58	4.87E-07	3.22E-06	15.50	1.89
CU6337W	298	6.45	0.58	2.82E-07	4.22E-06	15.50	2.45
CU6337X	298	6.45	0.32	1.06E-07	2.70E-07	15.50	1.71
CU63372C	298	6.45	0.58	3.33E-07	3.88E-06	15.50	2.25
CU63372B	298	6.45	0.58	2.08E-07	2.27E-05	15.50	1.31
CU63372D	298	6.45	0.32	2.48E-08	2.58E-09	15.50	1.66
BR6337R	298	30.45	0	2.11E-05	0	20.71	1.41
BR6337S	298	30.45	0	2.16E-06	0	20.71	1.44

Appendix 1. cont'd

Specimen ID	Temperature (K)	Tension Load (kg)	Torsion Load (kg)	Tension Min Creep Rate (s^{-1})	Torsion Min Creep Rate (s^{-1})	Average Von Mises Stress (MPa)	Effe Strair (s
BR6337O	298	30.45	0	1.33E-05	0	20.71	8.84
BR6337T	298	30.45	0	5.42E-05	0	20.71	3.61
BR6337U	298	30.45	0	2.92E-06	0	20.71	1.95
BR6337V	298	30.45	0	2.73E-06	0	20.71	1.82
BR6337W	298	30.45	0	2.36E-06	0	20.71	1.58
BR6337X	298	7.45	0	1.20E-09	0	5.07	8.00
BR6337Y	298	7.45	0	7.68E-10	0	5.07	5.12
BR6337Z	298	7.45	0	7.11E-09	0	5.07	4.74
BR63372A	298	0	0.65	3.43E-07	2.97E-06	16.90	1.73
BR63372B	298	0	0.65	8.35E-08	9.95E-07	16.90	5.77
BR63372C	298	0	0.65	1.25E-07	1.06E-05	16.90	6.10
BR63372D	298	0	0.65		2.90E-06	16.90	1.68
BR63372E	298	0	0.65	7.83E-08	6.31E-07	16.90	3.68
CU6337Y	298	0	0.65	9.08E-09	1.49E-06	16.90	8.59
CU6337Z	298	0	0.65	2.19E-09	2.45E-06	16.90	1.41
CU63372F	298	0	0.65	1.43E-07	9.21E-06	16.90	5.32
CU63372G	298	22.9	0	9.30E-06	0	15.57	6.20
CU63372H	298	22.9	0	9.79E-06	0	15.57	6.53
CU63372I	298	22.9	0	6.00E-06	0	15.57	4.00
CU63372M	298	22.96	0	1.22E-05	0	15.61	8.16
CU63372J	298	6.45	0.58	2.91E-09	2.09E-05	15.50	1.21
CU63372N	298	6.45	0.58	1.39E-06	6.57E-06	15.50	3.91
CU63372O	298	6.45	0.58	1.58E-06	6.32E-06	15.50	3.80
CU63372Y	298	6.45	0.58	4.66E-07	2.90E-06	15.50	1.70
CU63373B	298	12.45	0	1.36E-07	0	8.47	9.06
CU63373E	298	12.45	0	3.91E-07	0	8.47	2.60
CU63373R	298	12.45	0	1.29E-07	0	8.47	8.60

Appendix 1. cont'd

Specimen ID	Temperature (K)	Tension Load (kg)	Torsion Load (kg)	Tension Min Creep Rate (s^{-1})	Torsion Min Creep Rate (s^{-1})	Average Von Mises Stress (MPa)	Effe Strair (s
CU63373S	298	17.45	0	4.65E-07	0	11.87	3.10
CU63373T	298	17.45	0	4.06E-07	0	11.87	2.71
CU63373U	298	17.45	0	6.88E-07	0	11.87	4.59
CU63373V	298	19.95	0	1.00E-06	0	13.57	6.67
CU63373W	298	19.95	0	9.75E-07	0	13.57	6.50
CU63373X	298	19.95	0	2.57E-07	0	13.57	1.72
CU63373Y	298	29.95	0	1.02E-05	0	20.37	6.79
CU63373Z	298	29.95	0	8.04E-06	0	20.37	5.36
CU63374E	298	29.95	0	3.90E-06	0	20.37	2.60
CU63374C	298	9.95	0	1.27E-08	0	6.77	8.46
CU63374G	298	9.95	0	1.81E-08	0	6.77	1.20
CU63374D	298	9.95	0	6.06E-08	0	6.77	4.04
CU63375A	298	14.95	0	2.52E-07	0	10.17	1.68
CU63374R	298	14.95	0	2.84E-07	0	10.17	1.90
CU63375B	298	14.95	0	1.27E-07	0	10.17	8.46
CU63375C	298	14.95	0	9.79E-08	0	10.17	6.53
CU63375I	298	14.95	0	8.17E-08	0	10.17	5.45
CU63374Q	298	19.95	0	4.68E-07	0	13.57	3.12
CU63374Y	298	19.95	0	1.03E-06	0	13.57	6.89
CU63375D	298	19.95	0	1.25E-06	0	13.57	8.31
CU63375E	298	19.95	0	4.59E-07	0	13.57	3.06
CU63375H	298	8.45	0	8.00E-09	0	5.75	5.33
CU63375W	298	8.45	0	1.49E-08	0	5.75	9.91
CU63375O	298	7.45	0	1.06E-08	0	5.07	7.08
CU63375J	298	22.95	0	8.92E-07	0	15.61	5.95
CU63375K	298	22.95	0	1.21E-06	0	15.61	8.07
CU63375L	298	22.95	0	9.24E-07	0	15.61	6.16

Appendix 1. cont'd

Specimen ID	Temperature (K)	Tension Load (kg)	Torsion Load (kg)	Tension Min Creep Rate (s^{-1})	Torsion Min Creep Rate (s^{-1})	Average Von Mises Stress (MPa)	Effe Strair (s
CU63373LB	298	25.27	0	2.17E-06	0	17.18	1.45
CU63373JB	298	0	0.60	2.10E-07	4.04E-06	17.20	2.34
CU63372R	298	25.27	0	5.89E-06	0	17.18	3.93
CU63372T	298	25.27	0	1.34E-05	0	17.18	8.93
CU63373KB	298	25.27	0	3.65E-06	0	17.18	2.43
CU63376D	298	0	0.27	3.01E-09	1.64E-07	6.94	9.49
CU63376E	298	0	0.27	1.10E-07	1.39E-07	6.94	1.09
CU63376F	298	0	0.27	3.47E-09	7.38E-08	6.94	4.27
CU63376G	298	11.4	0.27	9.70E-08	1.36E-07	10.60	1.02
CU63376H	298	3.19	0.47	2.47E-07	1.76E-06	12.30	1.03
CU63376I	298	1.6	0.50	1.35E-07	1.82E-06	12.90	1.06
CU63376J	298	7.4	0.18	1.38E-08	2.03E-08	6.88	1.49
CU63376K	298	4.18	0.26	3.87E-08	9.16E-08	7.30	5.89
CU63376R	298	0	0.36	5.21E-09	4.85E-07	9.28	2.80
CU63376S	298	0	0.60	1.81E-07	6.17E-06	15.50	3.57
CU63376T	298	0	0.60	1.20E-09	4.55E-06	15.50	2.63
CU63376V	298	0	0.60	3.72E-08	7.52E-06	15.50	4.34
CU63376P	298	2.09	0.31	3.62E-08	2.11E-07	8.11	1.24
CU63376Q	298	0	0.36	2.08E-09	2.64E-07	9.30	1.52
CU63374H	373	9.95	0	6.04E-05	0	6.77	4.02
CU63374I	373	9.95	0	7.35E-05	0	6.77	4.90
CU63374J	373	9.95	0	6.17E-05	0	6.77	4.11
CU63374K	373	7.45	0	1.27E-05	0	5.07	8.45
CU63374L	373	7.45	0	7.67E-06	0	5.07	5.11
CU63374S	373	7.45	0	1.01E-05	0	5.07	6.73
CU63374P	373	7.45	0	1.06E-05	0	5.07	7.06

Appendix 1. cont'd

Specimen ID	Temperature (K)	Tension Load (kg)	Torsion Load (kg)	Tension Min Creep Rate (s^{-1})	Torsion Min Creep Rate (s^{-1})	Average Von Mises Stress (MPa)	Effe Strair (s
CU63373I	373	4.45	0	1.51E-06	0	3.03	1.01
CU63374M	373	4.45	0	1.35E-06	0	3.03	9.00
CU63374N	373	4.45	0	3.28E-06	0	3.03	2.19
CU63374O	373	4.45	0	1.70E-06	0	3.03	1.13
CU63374T	373	12.45	0	1.23E-04	0	8.47	8.21
CU63374U	373	12.45	0	5.66E-05	0	8.47	3.77
CU63374V	373	12.45	0	1.99E-04	0	8.47	1.33
CU63374W	373	12.45	0	4.78E-05	0	8.47	3.19
CU63374Z	373	2.45	0	4.66E-07	0	1.67	3.11
CU63374X	373	2.45	0	1.19E-06	0	1.67	7.91
CU63375F	373	2.45	0	6.79E-07	0	1.67	4.53
CU63375G	373	0.95	0	2.03E-08	0	0.65	1.35
CU63375X	373	0.95	0	2.75E-08	0	0.65	1.83
CU63375Y	373	0	0.27	4.31E-06	1.81E-04	6.76	1.05
CU63375Z	373	0	0.27	5.64E-06	2.44E-04	6.76	1.41
CU63376A	373	0	0.27	1.71E-07	2.42E-05	6.76	1.40
CU63376B	373	0	0.27	3.94E-06	1.74E-04	6.76	1.01
CU63376C	373	0	0.27	9.36E-06	2.95E-04	6.76	1.70
CU63376L	373	4.98	0.12	4.48E-06	6.58E-06	4.65	4.83
CU63376M	373	2.79	0.17	9.24E-07	4.14E-06	4.75	2.47
CU63376O	373	1.39	0.20	1.14E-06	1.24E-05	5.25	7.20
CU63376U	373	0.7	0.22	1.12E-06	3.07E-05	5.66	1.78
CU63376N	373	1.22	0.03	1.97E-08	1.28E-08	1.16	1.16
CU63376W	373	0	0.06	2.69E-08	7.41E-07	1.53	4.85

DISTRIBUTION

1	MS0824	A.C.Ratzel, 9110
1	MS0847	S.N. Burchett, 9126
1	MS0847	Harold S. Morgan, 9120
5	MS0889	B.L. Boyce, 1851
1	MS0889	T.E. Buchheit, 1851
1	MS0889	J. Mark Grazier, 1833
1	MS0889	F. Michael Hosking, 1833
1	MS0889	Jerome A. Rejent, 1833
1	MS0889	R.J. Salzbrenner, 1835
1	MS0889	John J. Stephens, Jr., 1833
1	MS0889	P.T. Vianco, 1833
1	MS0993	M.K. Neilsen, 9123
1	MS1076	Jonathan S. Custer, 1745
5	MS1411	H.E. Fang, 1834
1	MS1411	E.A. Holm, 1834
1	MS9403	N.Y.C. Yang, 8723
1	MS9401	Jill Hruby, 8702
1	MS9404	J.R. Garcia, 8725
5	MS9404	W-Y Lu, 8725
1	MS0188	D. Chavez, LDRD Office, 1030

1 Prof. C.L. Chow
Department of mechanical Engineering
University of Michigan-Dearborn
Dearborn, MI 48128

1 Prof. Y.-L.Shen
Department of mechanical Engineering
University of New Mexico
Albuquerque, NM 87131

3	MS 9018	Central Technical Files, 8945-1
1	MS 0899	Technical Library, 9616
1	MS 9021	Classification Office, 8511/Technical Library, MS 0899, 9616

DOE/OSTI via URL on page 2